Article:
McMaster, SJ orcid.org/0000-0002-7339-2469, Liskiewicz, TW, Neville, A et al. (1 more author) (2020) Probing fatigue resistance in multi-layer DLC coatings by micro- and nano-impact: Correlation to erosion tests. Surface and Coatings Technology, 402. 126319. ISSN 0257-8972

https://doi.org/10.1016/j.surfcoat.2020.126319

Probing Fatigue Resistance in Multi-layer DLC Coatings by Micro- and Nano-impact: Correlation to Erosion Tests

Samuel J. McMaster[a*], Tomasz W. Liskiewicz[a,1], Anne Neville[a], Ben D. Beake[b]

* Corresponding author: py11sjm@leeds.ac.uk

[a] School of Mechanical Engineering, University of Leeds, Leeds, LS2 9JT, UK

[b] Micro Materials Ltd., Willow House, Yale Business Village, Ellice Way, Wrexham, LL13 7YL, UK

[1] Present address: Faculty of Science and Engineering, Manchester Metropolitan University, John Dalton Building, Chester Street, Manchester, M15 6BH, United Kingdom

Abstract

DLC coatings have seen recent use as protective coatings for flow control devices in the oil and gas industries. Improving fatigue resistance for multi-layered DLC coatings on hardened steel is key for improving their performance in this harsh environment of highly loads repetitive contact. This has been studied directly by micro-scale repetitive impact tests at significantly higher strain rate and energy than in the nano-impact test, enabling the study of coating fatigue with spherical indenters and dry erosion testing. Nano-impact has also been used to assess the initial fatigue behaviour of the coatings. Good correlation between micro-impact results and erosion results was found. Hard multi-layered a-C:H and Si-a-C:H coatings were found to be significantly less durable under fatigue loading than a-C:H:W. The influence of the coating mechanical properties and structure on these differences is discussed. The results of this study provide further strong evidence that in highly loaded mechanical contact applications requiring a combination of load support and resistance to impact fatigue, the optimum lifetime of coated components may be achieved by designing the coating system to combine these properties rather than by solely aiming to maximise coating hardness as this may be accompanied by brittle fracture and higher wear.

Keywords: DLC, erosion, impact, nanoindentation, nanomechanics

1. Introduction

Diamond-like carbon (DLC) is used to describe a class of mechanically hard amorphous metastable carbon materials [1–3]. Properties of DLC can vary with the ratio of sp2 (threefold planar bonding) to sp3 (fourfold tetrahedral bonding) hybridised bonding and hydrogenation of the film [2,4,5]. In addition to high hardness, DLC films are characterised by chemical inertness and low coefficients of friction making them ideal wear resistant coatings [3,6]. High residual internal compressive stresses are common in harder DLC coatings, methods to reduce these stresses include the inclusion of metal doping into the DLC layer and presence of a functionally graded metallic to carbide interlayer [7–11]. The inclusion of dopants into DLC

structures can modify properties such as the hardness, tribological properties or internal stresses to tailor it for different operating environments [12]. Doping with silicon gives improved corrosion resistance and humidity and temperature stability [13]. The use of metal such as tungsten as a dopant can reduce internal stresses and improve film adhesion [14]. DLC can be deposited by various methods and precursors such as radio frequency (RF) or direct current (DC) chemical vapour deposition (CVD), magnetron sputtering and ion beam deposition. Plasma assisted CVD (PACVD) deposited films typically have greater levels of hydrogen content (up to 60 %) [3,6]. DLC films see many practical applications across industry including razor blades, MEMs devices, cutting tools and as protective coatings for mechanical combustion engines [1,3,15]. More recently, DLC coatings have been seen as a potential protective coatings of flow control devices in oil and gas pipelines [16]. In this application, fatigue resistance is key due to repetitive stresses of hard particle impacts, particularly, sand particle impacts.

Sand particles, suspended in water or entrained in airflow, can cause expensive erosion damage to both the internal and external surfaces of valves, pumps and pipework [17]. It is well understood that the erosion rate of a material is dependent on its relative brittleness/ductility in addition to the velocity and angularity of the erodent material [18]. Additionally, the impingement angle of the jet changes the erosion rate dependent upon the relative brittleness/ductility of the material [17,19]. Material chipping, cracking and removal are not the only considerations in erosion wear as the large number of particle impacts is a fatigue process [20–22]. Coatings for erosion applications such as for gas turbine blades typically consist of carbide or nitride metal ceramics however high velocity oxy-fuel (HVOF) coatings are also seen in marine applications where corrosion resistance is required too [23–27]. Metal nitrides are seen in use for aerospace applications; the erosion rate is seen to decrease with surface hardness for these coatings and multi-layers are seen to beneficial [21].

The shear stress maps modelled by Zhang et al. [28] support this with higher numbers of sandwich layers lowering the maximum shear stress and Von Mises stress. Due to DLC films nature as hard coatings, they will generally display brittle behaviour however this can change with differences in the sp2/sp3 ratio [2,4,5] and dopants [12] affecting the mechanical properties for varying coating structures. This allows DLC to be tailored to required properties to a greater degree than other coatings. Erosion testing under slurry or air conditions presents difficulties in analysing the wear rate of coatings due to the difficulties in setting up a test and stopping the test to analyse the amount of coating removed. This itself is difficult due to the low mass removal rates involved therefore other techniques such as optical analysis must be employed.

Bull [29] showed that indentation experiments can mimic processes observed in erosion and can be reasonable for the development of models. It was additionally noted that coating thickness should be chosen to match the energy of the erodent particles. A single indentation (with quasi-static loading), however, cannot mimic the high strain rates produced during impact or erosion testing [30]. Micro- and nano-impact allow for high strain rate testing and its repetitive nature is more representative of erosion under repeated particle impingement, which is particularly important as strain rate has been seen to affect the fatigue failure of thin PVD coatings [31]. Previous studies have identified the need in combining several techniques (such as nanoindentation, scratch and impact testing) to characterise a coating's mechanical properties to assess performance [32]. Impact testing (on both micro and nano scales) has been an emerging technique used to characterise the performance of coatings [33]. It can be useful to determine the fracture resistance of hard coatings [34,35] but can also be used to assess fatigue resistance under repetitive loading like the impacts of erosive particles [33,34,36–38]. Research is trending towards the measurement of dynamic hardness of surfaces and the use of different length-scales in testing to drive failure faster [30,37,39].

Additionally, the use of nanoindentation mapping to assess the dynamic changes in surface hardness has been seen particularly with fretting wear [40,41].

In this study, the hypothesis was that the progressive depths reached in impact testing can be compared with the amount of substrate revealed in erosion testing to show that instrumented impact can be used to predict erosion performance of coatings. Impact and particle impingement both present similar repetitive high strain rate fatigue wear to the coating surface allowing the two processes to be linked. Mechanical properties and structural information determined by Raman spectra were used to inform on the coating behaviour. By using an instrumented impact method, we can standardise the loading regimes tested on the coatings allowing us to control the conditions to a greater degree than with a slurry or air-based erosion test. Additionally, immediate depth information can be acquired from the impact test as opposed to the complex post-test analysis required for erosion testing.

2. Methodology

2.1. Materials

Three DLC coatings are studied on both 316L stainless steel (SS) and hardened M2 tool steel (HTS):

- a-C:H (Coating A).
- Si-a-C:H (Coating B).
- a-C:H:W (Coating C).

By using three coatings and two substrates with varying mechanical properties, a range of coating to substrate properties can be tested. Coating deposition was performed with the Hauzer Flexicoat 850 physical vapour deposition (PVD) and plasma assisted chemical vapour deposition (PACVD) system located in the School of Mechanical Engineering at the University of Leeds. Prior to deposition, the substrates were polished to a roughness of 0.01 µm R_a. Multiple substrates were prepared for each coating to allow for all the various testing

methods in this study. PVD was used to deposit the adhesive and gradient interlayers on the substrates (see Table 1 for the structure of the coatings). PACVD was used with acetylene (C_2H_2) as the precursor gas for the top DLC layer. Hexamethyldisiloxane (HMDSO), vaporized in the chamber during deposition, was utilized to achieve the doping necessary for Coating B. The engagement of a magnetron sputtering WC target provided the doping for Coating C. The same coating process was utilised for coating on both SS and HTS. The full details of the deposition procedures are given in Section 2.2. The difference in coating thickness can be attributed to the increased hardness of the tool steel substrate benefitting coating growth as less ion subplantation will occur before true film growth [42].

The Calotest technique involves rotating a large diameter (30 mm for this testing) steel ball against the coating surface until the top layer of coating is worn away. Several drops of nanocrystalline diamond suspension is used to aid in the wear due to the hardness of the coating. Optical microscopy is then used to measure the dimensions of the crater [43]. Table 1 shows the coating layer design and measured thickness for each layer.

Table 1. Multilayer coating architecture design with interlayer and top layer DLC. The DLC layer thickness has been measured by calotest and FIB cross-section SEM.

Substrate	Coating	Layer Structure	Adhesive (Cr) layer (µm)	Gradient Layer (µm)	DLC layer (µm)	Total (µm)
316L Stainless Steel	a-C:H (A)	Cr+WC/W-C:H+DLC	0.29 ± 0.03	0.89 ± 0.08	1.60 ± 0.17	2.65 ± 0.19
	Si-a-C:H (B)	Cr+WC/W-C:H+DLC	0.29 ± 0.03	0.89 ± 0.08	1.16 ± 0.24	2.21 ± 0.25
	a-C:H:W (C)	Cr+WC+DLC	0.29 ± 0.03	0.29 ± 0.06	1.10 ± 0.22	1.65 ± 0.23
Hardened M2 Tool Steel	a-C:H (A)	Cr+WC/W-C:H+DLC	0.29 ± 0.03	0.89 ± 0.08	2.20 ± 0.20	3.25 ± 0.22
	Si-a-C:H (B)	Cr+WC/W-C:H+DLC	0.29 ± 0.03	0.89 ± 0.08	2.17 ± 0.16	3.22 ± 0.18
	a-C:H:W (C)	Cr+WC+DLC	0.29 ± 0.03	0.29 ± 0.06	1.17 ± 0.12	1.72 ± 0.14

2.2. Coating Deposition Procedure

The sequence of deposition steps to produce the coatings can be summarised as:

(i) Chamber heating

(ii) Target cleaning

(iii) Plasma surface etching

(iv) Cr layer deposition

(v) Cr/WC deposition

(vi) a-C:H:W deposition (final step for Coating C)

(vii) a-C:H/Si-a-C:H deposition (for Coatings A and B respectively)

The conditions for each step are summarised in Table 2. In the first step, the chamber is pumped to 4 x 10^{-5} mbar and heated to 200 °C. The heaters are engaged again in the plasma surface etching step otherwise the temperature is not controlled during deposition. The pump was maintained at low power throughout deposition to evacuate waste gases from the chamber. The bias voltage utilises DC current during the target cleaning step, low pulse current (PLS low) in the plasma surface etching step and high pulse current (PLS high) in the a-C:H and Si-a-C:H deposition steps. C_2H_2 and HMDSO flow rates have a time ramp as specified in the relevant columns.

Table 2. Coating deposition step parameters.

Deposition Step/Conditions	Temperature (°C)	Pressure (x10^{-5} mbar)	Bias Voltage (V)	Cr target power (kW)	WC target power (kW)	Ar flow rate (sccm)	C_2H_2 flow rate (sccm)	HMDSO flow rate (sccm)	Table rotation speed (rpm)	Time (mins)
Chamber heating	200	4	-	-	-	-	-	-	1	60

Target cleaning	-	-	500 (DC)	6	3	130	-	-	2	20
Plasma surface etching	150	-	200 (PLS low)	-	-	50	-	-	2	45
Cr deposition	-	-	-	3	-	130	-	-	3	25
Cr/WC deposition	-	-	-	3	3	110	-	-	3	30
a-C:H:W deposition	-	-	-	-	3	90	8-30 (30 mins)	-	3	75 (A & B) 120 (C)
a-C:H deposition	-	-	740 (PLS high)	-	-	-	380-270 (8 mins)	-	1.5	150
Si-a-C:H deposition	-	-	740 (PLS high)	-	-	-	200-120 (8 mins)	18-12 (8 mins)	1.5	120

2.3. Nanoindentation

Partial loading nanoindentation under load control was carried out using a Nanotest Vantage nanoindentation system with a Berkovich diamond indenter. A total of 10 indentations with 40 loading points, in a range of 0-500 mN, per sample, was used to characterise the change in

mechanical properties with depth in the coating system. Indentations were performed prior to other testing on unworn areas on coated substrates dedicated to nanoindentation. The load and unload time for each indentation step was 2 seconds. A 1 second dwell was used at the maximum load to ensure there was no creep. A 60 second dwell period in the final unload step was used for thermal drift correction. The area function of the indenter was found by indentation into a fused silica reference sample. Hardness (*H*) and elastic modulus (*E*) were calculated by applying Oliver-Pharr analysis [44]. *E* and ν (0.2) are Young's modulus and Poisson's ratio for the coating; E_i (1140 GPa) and ν_i (0.07) are the same quantities for diamond respectively [45].

2.4. Scratch testing

Progressive loading scratch testing was performed with a Tribotechnic Millennium 200 scratch tester to assess the coating adhesion. A load of 0-50 N was used with a loading speed of 100 N/minute and a scratching speed of 10 mm/minute. A 200 µm radius diamond Rockwell C indenter was used for testing. L_{C1} and L_{C2} loading points were analysed. The larger scale scratch test (compared to nano-scratch) was performed to assess the cracking resistance of the total coating structure. Smaller probe radii could be used to study inter-layer cracking phenomena [46]. A typical scratch as seen on SS Coating A is seen in Figure 1. Spallation is seen at L_{C1} with chevron cracking appearing before and continuing after indicating a brittle failure. Tensile cracking is seen at L_{C2}. Gross spallation is seen near the maximum load of the scratch [47].

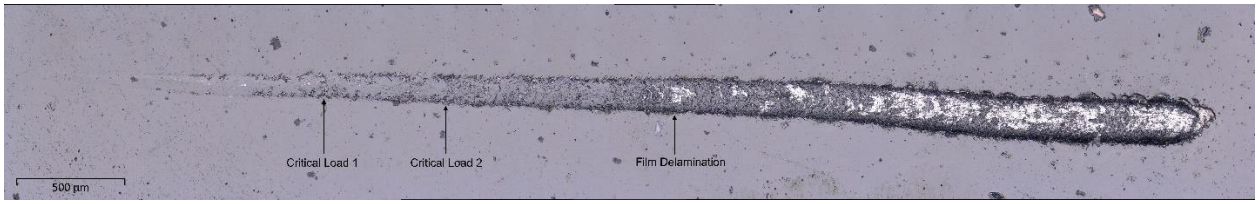

Figure 1. Scratch test of SS Coating A with critical loads and film delamination annotated.

2.5. Raman Microscopy

A Renishaw Raman microscope was used to determine the I_D/I_G ratio to provide an estimate of the amorphisation of the carbon within the coatings [48,49]. In addition to the pre-test baseline readings, on samples where the impact sites could be located, spectra were taken inside the craters of the 1 N loads.

A 488nm laser was used to target a Raman frequency range of 1000-2000 cm^{-1}. In this frequency range, we observe a dual peak phenomenon. The D peak is around 1350 cm^{-1} and the G peak is around 1580-1600 cm^{-1} [48,50]. The G band peak is due to the stretching of all bond pairs in sp^2 atoms (present in both chains and rings) and the D band is caused by the breathing modes of sp^2 atoms in rings [51,52]. The ratio of the areas of the peaks gives the amount of sp^2 hybridised bonding located in rings [53] with higher values indicating higher sp^2 content. From this, we can infer that in coatings with higher I_D/I_G ratio there is less sp^3 content. Gaussian fitting with ratios of the peak area was used for these spectra as opposed to the Lorentzian with full width half maxima [48]. Baseline subtraction and peak fitting was performed using OriginPro. The diameter of the Raman laser on the surface is determined by the Airy disk equation [54]. For a 488nm laser, we find a theoretical diameter of 397nm using a 0.75/50x lens.

2.6. Impact testing

2.6.1. Micro/nano-impact

Micro-impact testing was used with varying loads (400-1000 mN with a time of 300 secs) to characterise the fatigue and fracture resistance of coating systems. A sphero-conical indenter of 12-15 µm radius (dependent on depth from apex) was used. A Micro Materials Vantage system with a micro-loading head (0.4 - 5 N) was used for impact testing. A solenoid is connected to timed relay was used to produce repetitive impacts on the coating surface; computer control ensures that each impact was in the same location for each load and occurs

every 4 seconds [32,39]. Maximum testing time was 300 seconds resulting in 75 impacts in the test duration. Three repeats, where possible, were used in different locations on the sample. Loads of 400, 500, 600, 650, 700, 750 and 1000 mN were specified for this testing. In all impacts, the indenter was retracted 40 µm from the surface.

Several features across the impact depth maps of the coatings can be highlighted to compare the performance of the coatings across the selected loads. These parameters are:

- I_0 – quasi-static depth.
- I_1 – the depth of the first true impact.
- I_f – the depth of the final impact.
- I_δ – the ratio of final depth to initial depth normalised by the initial impact depth. This parameter shows the relative level of fatigue (depth increase due to crack formation) between each loading step.

I_δ is defined by:

$$I_\delta = \frac{I_f - I_1}{I_1} \quad (1)$$

Nano-impact at 100 mN load with 75 impacts (corresponding to 300 seconds) was used to probe initial cracking behaviour of the coatings. 3 repeats were performed to ensure repeatability. The same indenter geometry of 12-15 µm was utilised for this testing. A retraction distance of 15 µm was used for nano-impact tests. The nano-loading head has a range of 10-100 mN when used in impact mode.

2.7. Erosion Testing

Due to the induction period of initial mass gain in erosion tests, mass loss was unable to be used to calculate the amount of coating removed in erosion. Mass gain is erosive conditions is seen in several materials at high impingement angles (>45°) due to embedding of particles [19,55–57]. Image analysis to distinguish between the exposure of different layers is used

instead.

Sand particles (of average size 250 µm) were used in an air-based erosion testing of the coatings at 90° impingement angle. Erosion tests were performed in a bespoke air erosion rig as seen in Figure 2. Speed of the particles was determined by dual exposure high shutter speed photography. The velocity was calculated by taking the distance travelled by the sand particles seen as a streak in the photograph measured with a pixel to distance conversion, and the time by the exposure time of the photograph. The speed was calibrated to 15ms^{-1}.

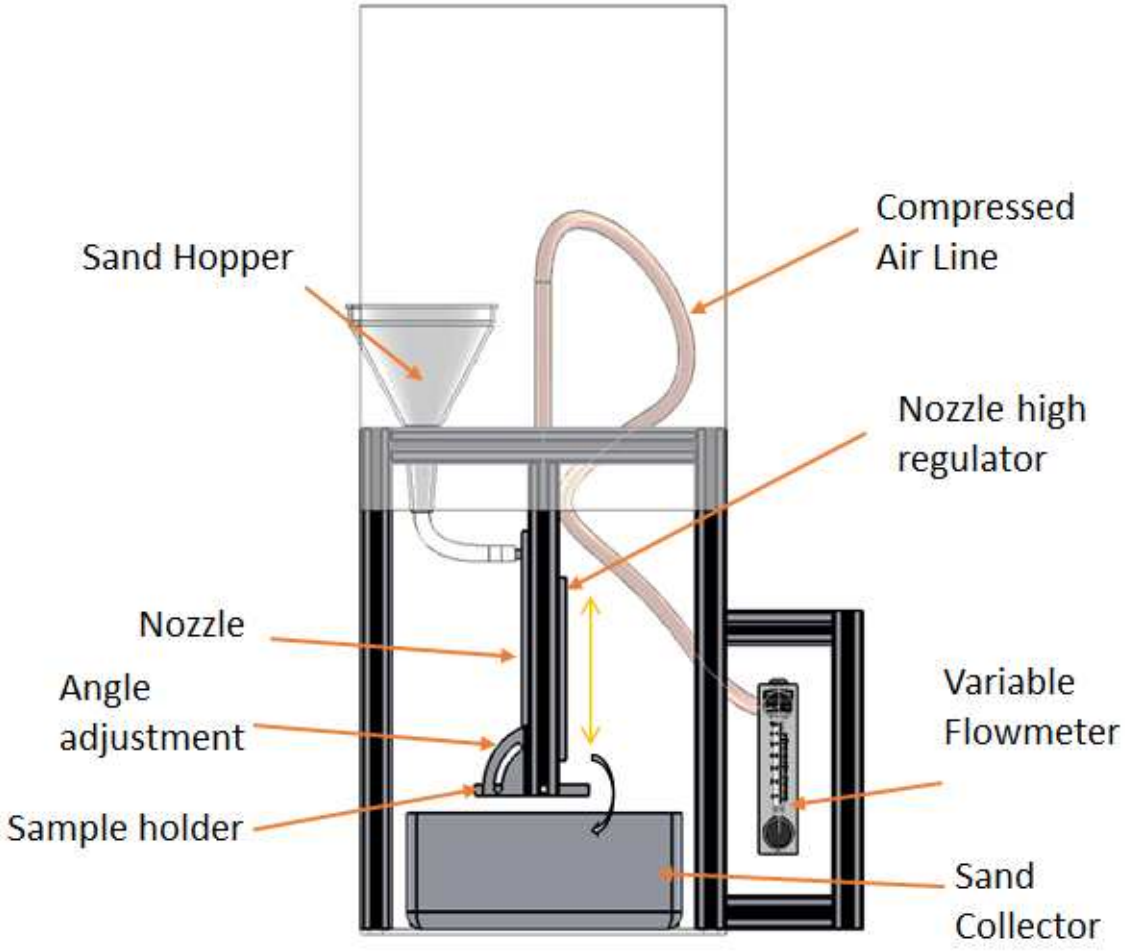

Figure 2. Schematic of the bespoke air erosion rig.

Erosion tests were performed for the required times and analysed after each time step with 5 images captured of each erosion wear scar. The images were converted to 32-bit black and

white images and the pixel threshold in ImageJ was used to highlight differently shaded areas corresponding to the exposure of the substrate. An area calculator was then used to find the amount of substrate exposed. A similar method was employed by Bouzakis et al. [58] to find the failed area ratio of impact tests. In Figure 3, lighter areas of the image corresponds to the substrate visible after material removal due to erosion of the coating.

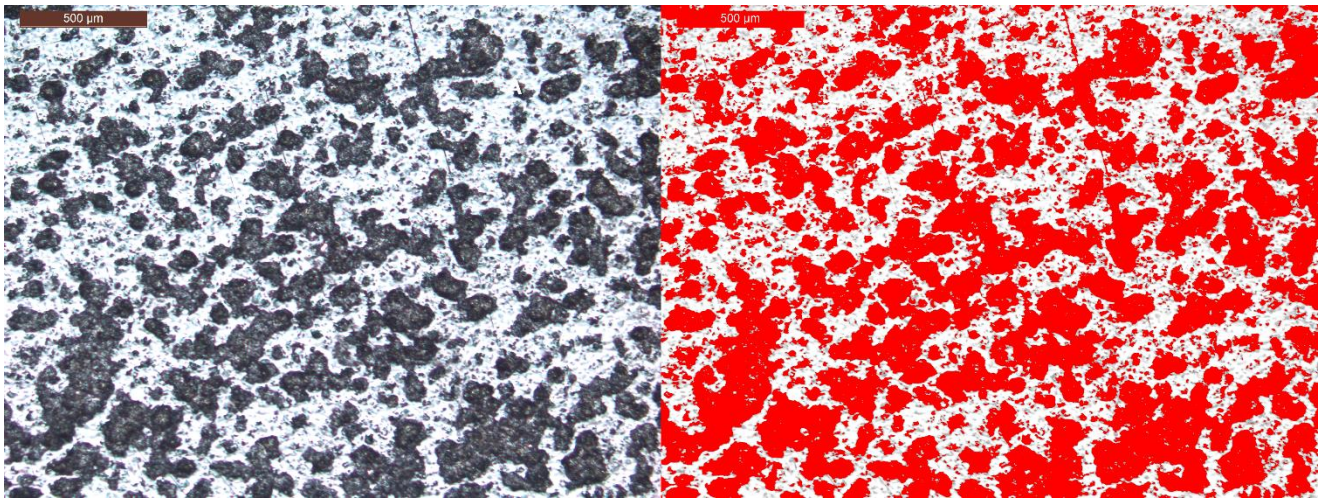

Figure 3. Left: Coating A after 90 seconds of erosive particle impacts. Right: Image after pixel thresholding technique has been applied. Light material is the substrate and darker material is the coating.

2.8. SEM Analysis

Cross-section SEM images were obtained by focused ion beam using a FEI Helios G4 CX Dualbeam SEM located in LEMAS (Leeds Electron Microscopy and Spectroscopy Centre). Platinum is deposited on the surface on the sample to protect it during material removal. The sample is tilted, and a beam of gallium ions is used to mill into the surface to reveal the substructure of the coating. An Oxford Instruments Aztec EDX (electron diffraction x-ray spectroscopy) system was used to identify the composition of cross-section layers. Unworn areas were chosen to analyse the thickness and composition of the coatings and interlayers. Impact craters were cross sectioned to inspect the sublayer cracking present under cyclic loading after 75 impacts at the maximum micro-impact load of 1 N and thereby discern the differences in behaviour between the DLC coatings similar to the work of Abdollah et al.

[59,60] but in a more qualitative sense due to the on load depth already being measured by the NanoTest Platform.

3. Results

3.1. Mechanical Properties

Surface mechanical properties of the coatings are determined by extrapolating partial loading nanoindentation to the surface (zero contact depth). The elastic modulus (E) is determined by taking the mean of the maximum range to negate surface contact effects reducing the modulus at low contact depths. Hardness (H) is found by extrapolating the maximum to the y-axis to give the surface hardness [61].

Table 3 shows the nanoindentation and scratch test data for both the coated and uncoated substrates. The substrates show distinct differences in their mechanical properties with HTS having surface hardness with a value of 10.0 GPa compared to 2.6 GPa for SS. However, the mean elastic modulus is slightly higher with a value of 223 GPa. This results in HTS having higher values of both H/E and H^3/E^2 (0.042 and 0.017 GPa respectively). The mechanical properties of the SS substrate are similar to that recorded by Ward et al. [62] prior to coating with a-C:H with Si interlayer. The hardness of the HTS after hardening is similar to that seen by Wilbur et al. [63] though a nitriding processing was used compared to the flame hardening for this study. Coating A has the highest hardness value when deposited on both substrates with values of 19.4 GPa and 20.2 GPa on SS and HTS respectively. The highest mean elastic modulus is seen on Coating C on both substrates with values of 235 GPa and 218 GPa for SS and HTS respectively.

Leyland and Matthews proposed that utilising the ratio of hardness (H) to elastic modulus (E) modulus for coatings (H/E) was a key parameter in evaluating a coatings wear resistance [64]. Though this was recognised by previous authors for alternative materials, this paper

introduced the concept for coating studies. Additionally, H^3/E^2 has become popular for evaluating the wear resistance of coatings however this is generally taken as a fracture toughness metric [65]. These parameters are generally used to rank coating performance.

The variance in coating thickness may play a part in the difference of Scratch Crack Propagation Resistance (or Scratch Toughness as called by Zhang) (CPR_S, $L_{c1}(L_{c2}\text{-}L_{c1})$) [66,67] measured across all the coatings particularly on Coating C deposited on HTS which has approximately 1 µm thinner top layer DLC. In general, we see a larger CPR_S for the coatings deposited of HTS versus SS. On SS the highest value of CPR_S is for Coating C with a value of 241 N^2. This compares to 71.1 N^2 and 175 N^2 for Coatings A and B respectively. The values for CPR_S on HTS for Coatings A and B are extremely similar with values of 281 N^2 and 280 N^2 respectively. Coating C has a slightly lower value of 206 N^2.

Table 3. Mechanical properties of three coatings on both substrates and mechanical properties of substrates. Hardness, Elastic modulus, H/E, H^3/E^2, L_{C1}, L_{C2}, CPR_S ($L_{C1}(L_{C2}\text{-}L_{C1})$).

Substrates	Coating	Surface Hardness (GPa)	Mean Elastic Modulus (GPa)	H/E	H^3/E^2 (GPa)	L_{C1} (N)	L_{C2} (N)	CPR_S $L_{c1}(L_{c2}\text{-}L_{c1})$ (N^2)
316L Stainless Steel	Uncoated	2.6	223	0.012	0.0004	N/A		
	A	19.4	215	0.090	0.158	27.54 ± 3.67	30.12 ± 1.63	71.1
	B	18.3	187	0.098	0.176	23.58 ± 2.30	30.99 ± 0.71	175
	C	16.2	235	0.069	0.077	24.11 ± 3.19	34.12 ± 2.20	241
Hardened M2 Tool Steel	Uncoated	10.0	204	0.042	0.017	N/A		
	A	20.2	199	0.101	0.207	23.68 ± 2.72	35.55 ± 2.97	281
	B	13.1	164	0.080	0.083	27.19 ± 2.25	37.50 ± 1.22	280
	C	13.9	218	0.064	0.056	22.10 ± 1.77	31.41 ± 1.28	206

Figure 4 a) and b) show the maps of *H/E* ratio varying with contact depth. Due to the binning process in which the data is averaged into 50 steps across the range of contact depth, some variance is expected, depending upon the depth reached for each loading step, thereby resulting in SS Coating A appearing to skip the first point. This data binning shows that on HTS (Figure 4 b)), the spacing between each point is smaller than that on SS due to the lower penetration of each indentation step. This indicates a greater amount of load support from the HTS substrate due to the smaller penetration with each repetitive indentation. In indentations on both substrates, the elastic modulus does not decrease to a large degree throughout the range of contact depth due to contact stiffness being less affected by surface roughness and indentation depth [61,68]. Thereby, we can surmise that the decrease in *H/E* ratio with contact depth is due to the decrease in hardness at higher contact depths as more substrate effects are seen [69]. Due to the thinner coatings of SS, the substrate effects are seen at lower contact depths.

On average, Coating A is seen to have the highest *H/E* ratio on both HTS and SS due to consistently higher hardness compared to the elastic modulus. However, it does appear to have a lower *H/E* at lower contact depths. This is because of initial elasticity in the contact due to the mean contact pressure being lower than the hardness of the film [46,61] with some surface roughness effects resulting in lower measured hardness at low contact depth [70]. However, it should be noted that this lower hardness at low contact depth, rise to plateau and fall off due to substrate effects is normal and is noted as a validity check by Fischer-Cripps [61]. Coating B is therefore seen to have a smoother surface finish resulting in higher *H/E* at low contact depth. Lower measured hardness except at lower contact depths results in a lower *H/E* values compared to Coating A. Coating C sees the consistently lowest *H/E* values due to its high elastic modulus throughout the contact depth range measured. These trends in H/E ratio follow that seen by Beake et al. [46] on similarly coated systems.

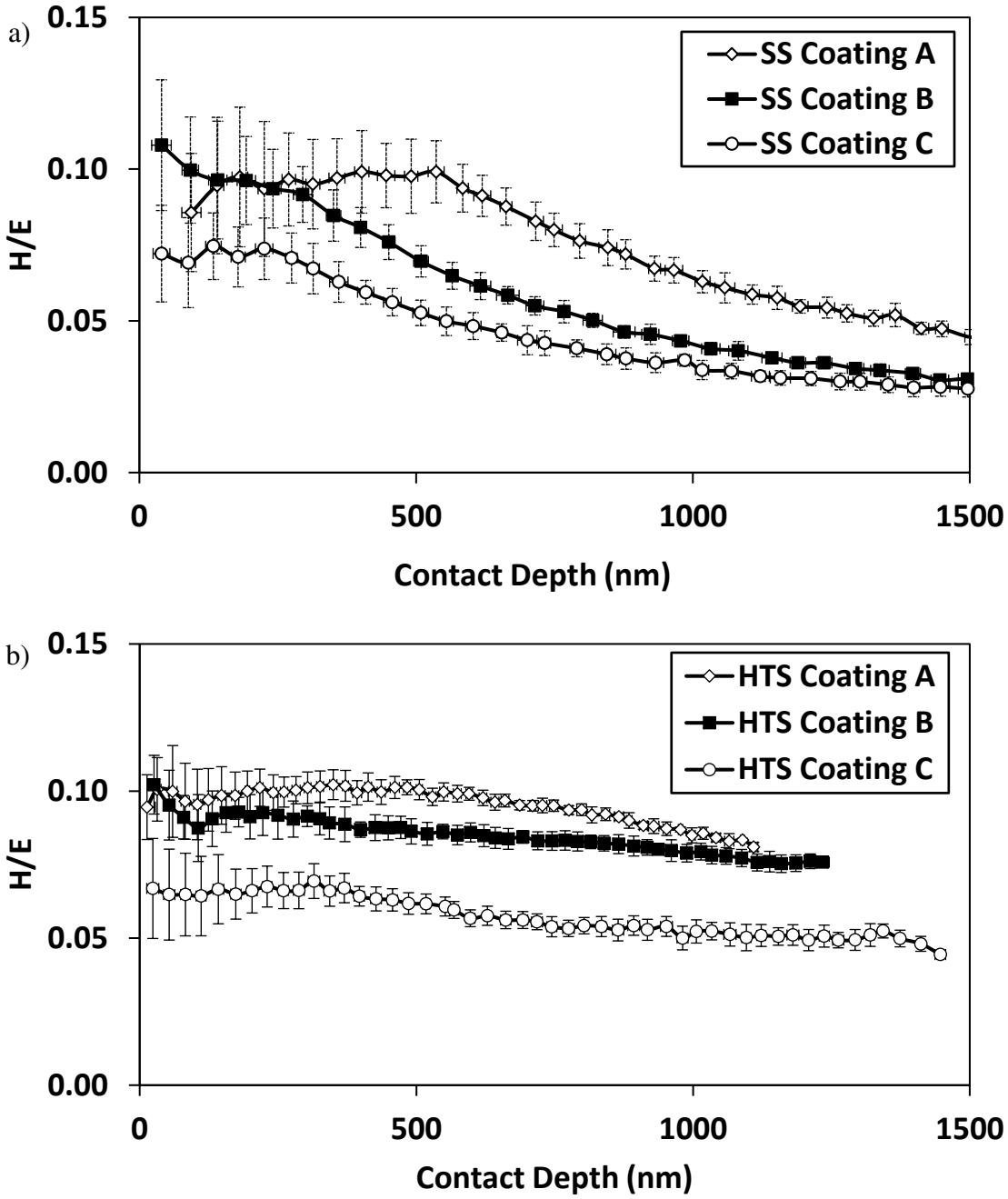

Figure 4**.** *H/E* ratio varying with depth into the coating system on a) SS and b) HTS.

3.1. Composition of the DLC layers

Table 4 shows the atomic composition of unworn areas of the coatings as measured by EDX before any FIB cross-sectioning was performed. The EDX analysis shows the presence of trace elements unintended to be constituents of the coatings. In the case of Ar as seen in SS

Coating B and Coating C on both substrates, some ions are embedded in the coating structure during deposition. Some amounts of Ti and O in HTS Coating C can be attributed to deposition of ions on the chamber walls from previous coating processes; Ti is used to re-coat the chamber between coating cycles using a cathodic arc process. Cr and Fe (and W in Coatings A and B) are detected due to the interaction volume of the electron beam [71]. Some variance in the unintended elements will be due to the thickness of the coatings. Coating A on HTS and SS has ~99.9 % and ~99.8 % carbon composition, respectively. Coating B consists of approximately 72.1 % and 71.1 % carbon, 6.9 % and 6.1 % oxygen, and 20.8 % and 21.9 % silicon on HTS and SS respectively. Coating C has the greatest difference in composition between HTS and SS. SS has ~79.3 % carbon compared to ~68.3 % as deposited on HTS. HTS Coating C has a larger proportion of W (~21.1 %) compared to SS (~16.31 %).

Table 4. Atomic composition of Coatings A, B and C on HTS and SS as measured by EDX. Measurements were made on unworn areas prior to FIB cross-sectioning.

	Atomic Composition (%)					
	Coating A		Coating B		Coating C	
Element	HTS	SS	HTS	SS	HTS	SS
C	99.90	99.80	72.06	71.12	68.29	79.33
O	-	-	6.88	6.13	5.93	-
Si	-	-	20.84	21.92	-	-
Ar	-	-	-	0.06	0.89	0.92
Ti	0.02	-	-	0.10	3.04	2.27
Cr	0.02	0.06	0.04	0.17	0.19	0.40
Fe	0.03	0.11	0.11	0.19	0.53	0.78
W	0.02	0.03	0.07	0.32	21.14	16.31

3.2. FIB-SEM cross-section

Figure 5 shows the FIB-SEM cross-sections of the unworn areas. These images were taken to corroborate the thickness measured attained by calotesting and to show the microstructure of the coatings and interlayer system. Therefore, this was only performed on one of the substrates, the same substrate used for Figure 10. The globular structure at the front of the milled area in Figure 5b) is due to redeposition of material from the ion beam. Additionally, a Mo and V concentration can be seen at the surface of the steel and proceeding into the microstructure. The insert EDX map of Figure 5c) shows the gradient layer present in Coating C compared to the distinct interlayer structure of Coatings A and B seen in subfigures a) and b) respectively.

a)

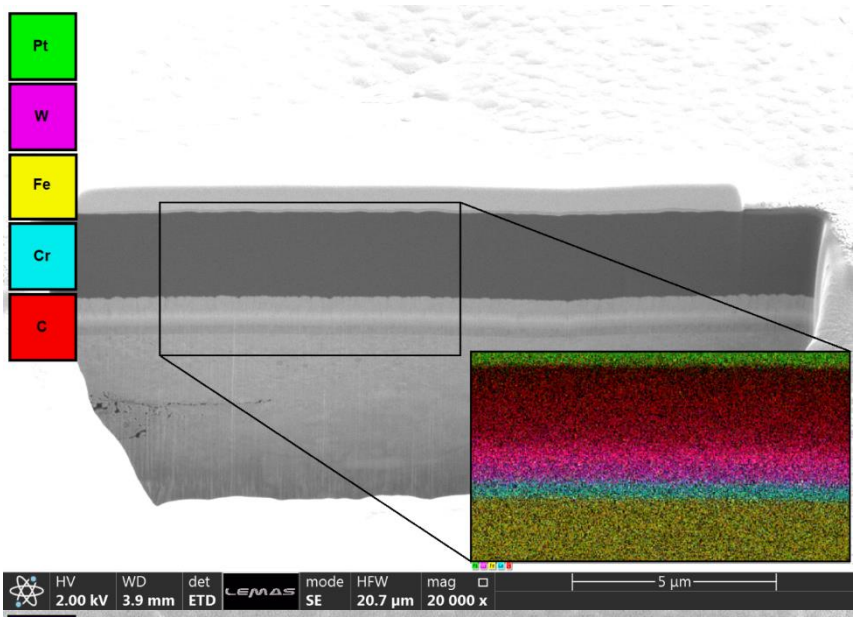
Pt
W
Fe
Cr
C
HV 2.00 kV
WD 3.9 mm
det ETD
mode SE
HFW 20.7 µm
mag 20 000 x
5 µm

b)

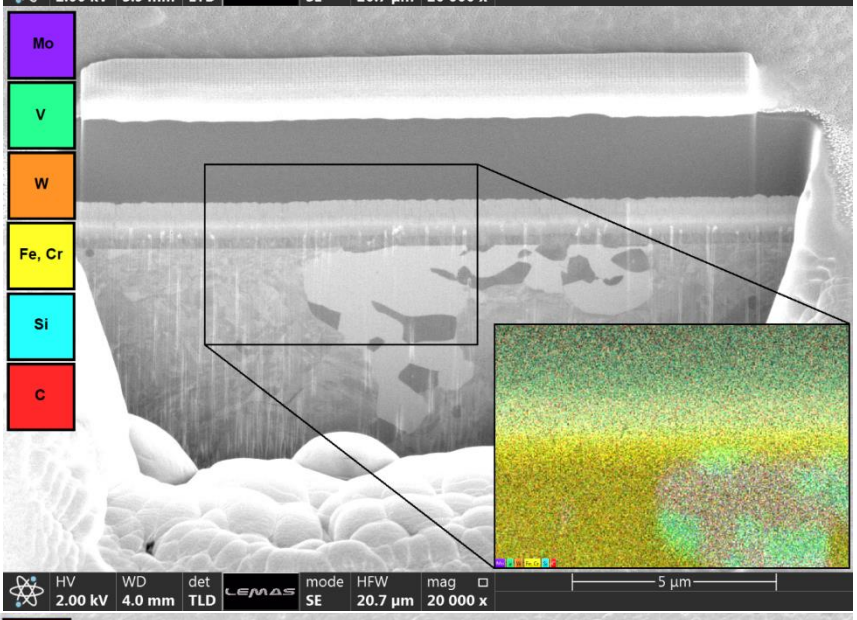
Mo
V
W
Fe, Cr
Si
C
HV 2.00 kV
WD 4.0 mm
det TLD
mode SE
HFW 20.7 µm
mag 20 000 x
5 µm

c)

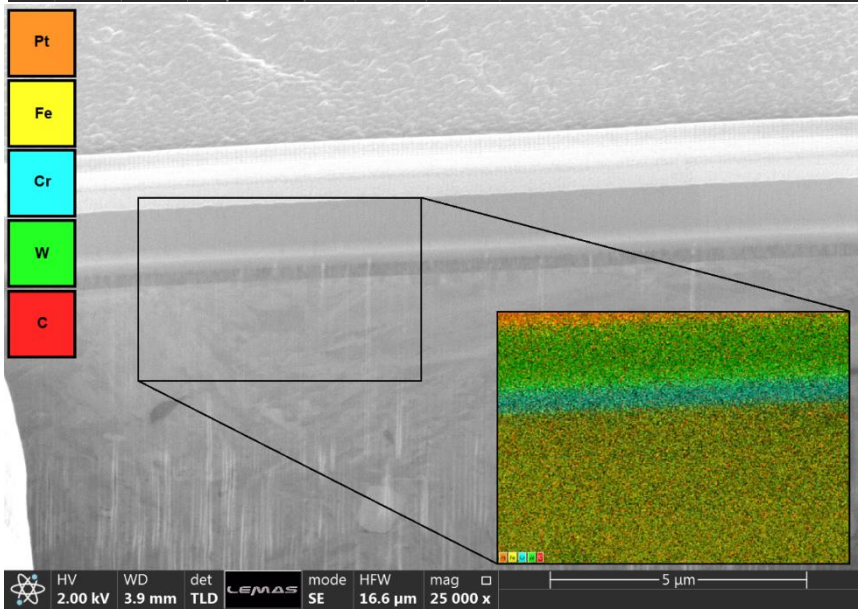
Pt
Fe
Cr
W
C
HV 2.00 kV
WD 3.9 mm
det TLD
mode SE
HFW 16.6 µm
mag 25 000 x
5 µm

Figure 5. Cross-section of coatings on HTS. Insert is an EDX map of the exposed cross-section. a) Coating A b) Coating B c) Coating C.

3.3. Raman Spectra

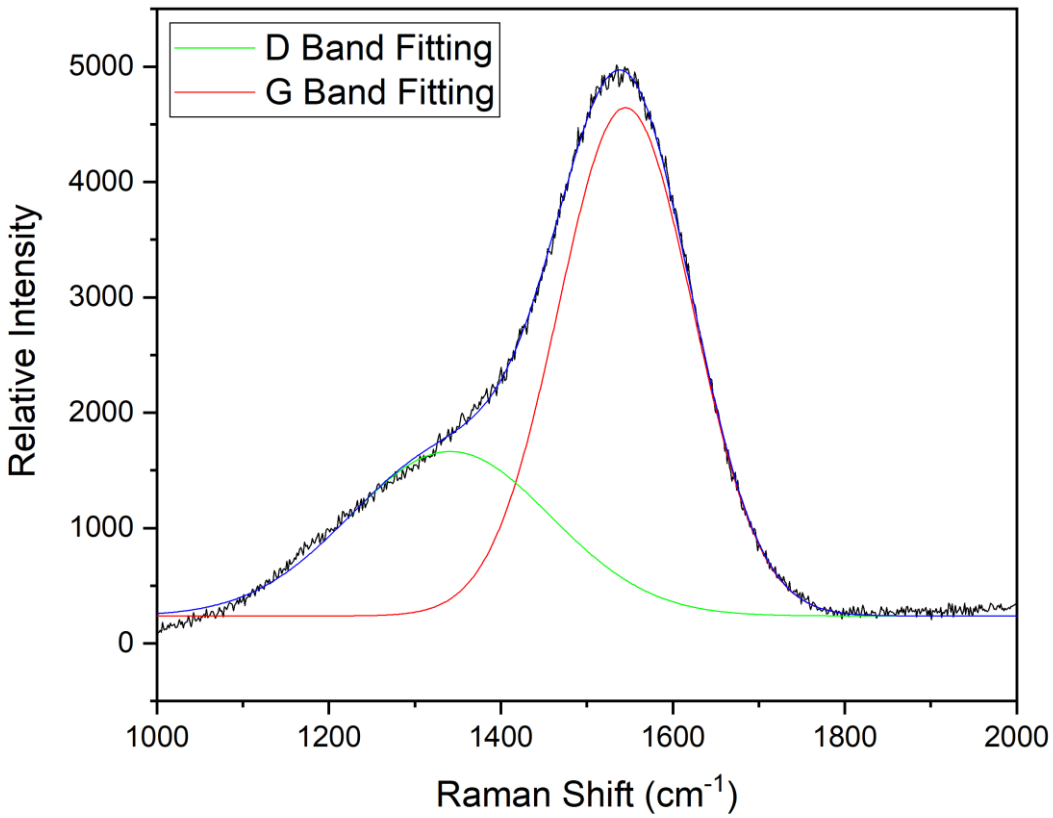

Figure 6 shows the fitting of the D and G band peaks of Coating A on HTS. Table 5 gives the calculated I_D/I_G ratios of all three coatings on both substrates pre- and post-test. The lowest pre-test values of I_D/I_G are seen on Coating B for both substrates (0.68 and 0.29 on SS and HTS respectively) indicating the lowest levels sp^2 carbons present in rings and therefore the lowest amorphization. The pre-test I_D/I_G values are lower on all coatings on HTS indicating that the increased hardness of the substrate gives a lower amorphization. The pre-test values of I_D/I_G on Coating C are much higher on both substrates (3.50 and 2.96 on SS and HTS respectively) indicating a highly disordered structured rich in sp^2 carbon [72]. The I_D/I_G values are approaching that seen by Yong et al. [72] indicating a structure more like graphitic-like carbon (GLC). Additionally, they identified a closely packed nano-particulate structure [72].

This would be similar to that seen by Pei et al. [73] with nano-crystallites of WC or W_2C [72] surrounded by an amorphous matrix. The post-test results for coating B on HTS show a marked increase in I_D/I_G indicating graphitisation due to impact where coating C decreases in I_D/I_G suggesting higher sp^3 content and destruction of larger sp^2 clusters [74,75].

Table 5. I_D/I_G ratio of Coatings A, B and C on each substrate.

Substrate	Coating	Structure	I_D/I_G (Pre-test)	I_D/I_G (Post-test)
316L Stainless Steel	A	a-C:H	0.79	-
	B	Si-a-C:H	0.68	-
	C	a-C:H:W	3.50	-
Hardened M2 Tool Steel	A	a-C:H	0.48	-
	B	Si-a-C:H	0.29	0.39
	C	a-C:H:W	2.96	1.61

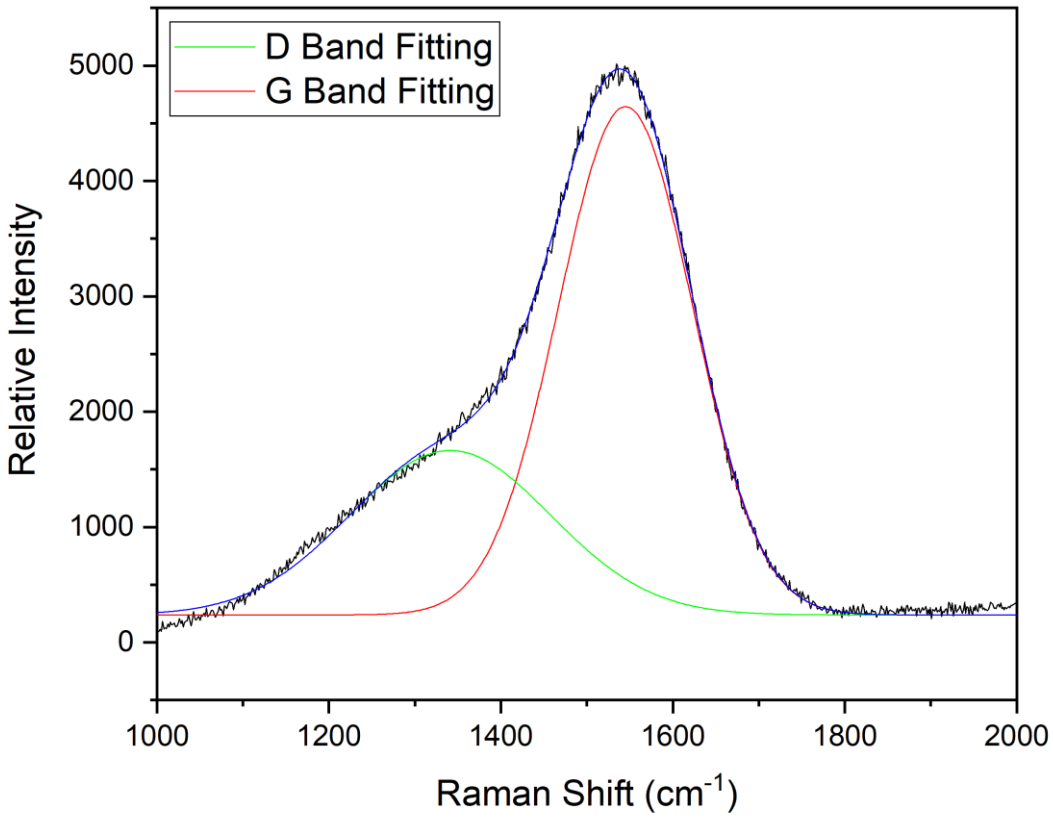

Figure 6**.** Fitting of D and G band peaks on Raman spectra of Coating A on HTS.

3.4. Micro-impact analysis

The progressive depth increase in micro-impact testing with 75 impacts at an impact load of 750 mN is seen in Figure 7. This is representative of the raw data in an impact test. SS Coating A fails at the first impact with a depth of 8776 nm reached showing that the load support of the substrate is insufficient for this system.

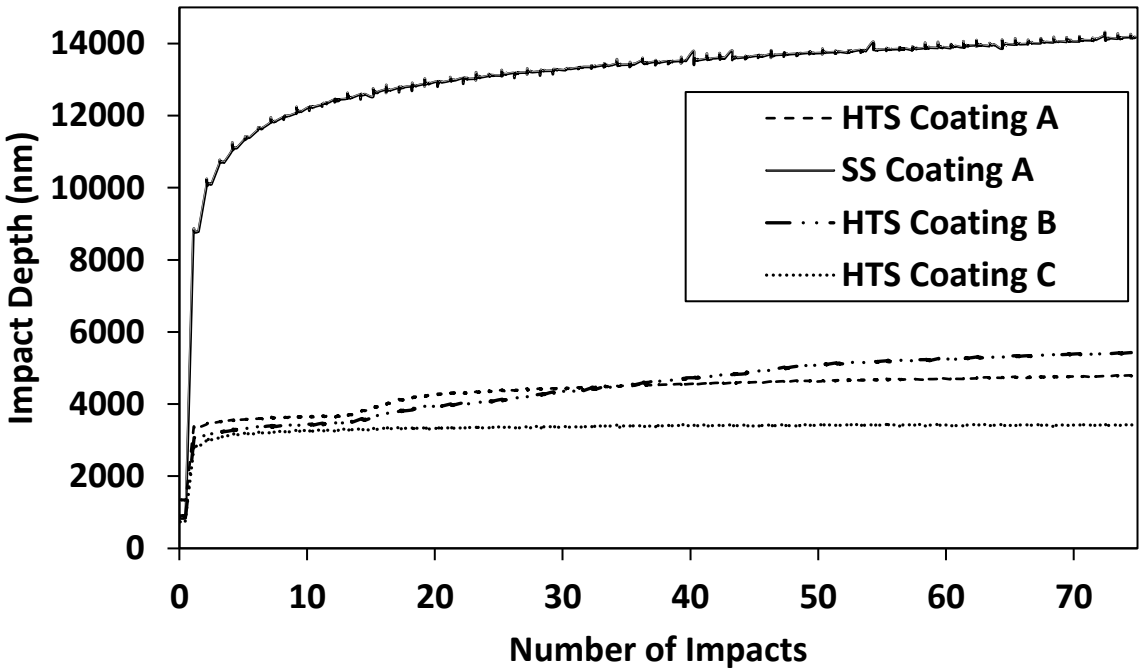

Figure 7. Representative micro-impact depth against number of impacts of 3 coatings on HTS and Coating A on SS. Impact load = 750 mN. Maximum number of impacts = 75 (300 seconds of testing).

Table 6 shows the number of impacts on HTS in which failure occurred against the number of full tests performed. Failure is defined by a sudden increase in depth within a short period of impact testing as with HTS Coating B (beginning at 14 impacts) in Figure 7. It can be noted that Coating C on HTS is less prone to failure across the full load range suggesting an increased fatigue resistance. Testing on coated SS coupons revealed eggshell type failures (immediate penetration of the coating and interlayers) under all impact loads [76], therefore

they are excluded from this table. Figure 7 demonstrates this behaviour with SS Coating A reaching 8760 nm at second impact.

Table 6. Number of impacts tests in which fatigue failure of the coating systems occurs against the number of tests performed.

Substrate and Coating / Impact Load	400 mN	500 mN	600 mN	650 mN	700 mN	750 mN	1000 mN
HTS Coating A	0/1	0/1	2/3	0/3	1/3	1/1	1/1
HTS Coating B	2/3	3/3	3/3	2/3	2/3	2/3	2/3
HTS Coating C	1/3	0/3	1/3	0/3	1/3	0/3	1/3

Figure 8 shows the impact parameters evaluated at each load tested. I_0 is similar across all the tests but is noticeably higher in Coating A as opposed to C. This is due to the initial crack formation in this coating at these loads. The initial and final depths reached throughout the testing is greater in Coating A and B additionally. Some degree of variability is seen in the final impact depths reached across the load range as is typical of the stochastic response for a fracture dominated process [39,77].

a)

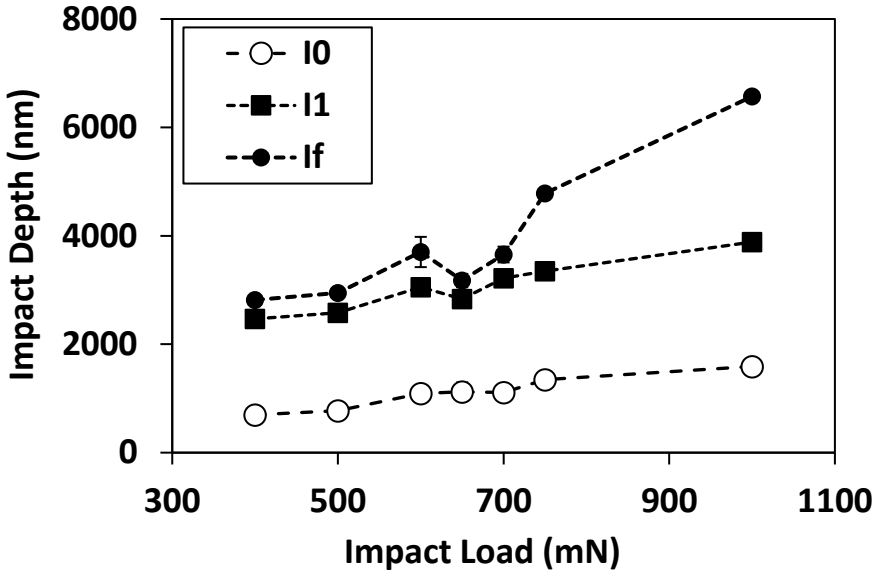
8000
6000
4000
2000
0
Impact Depth (nm)
I0
I1
If
300
500
700
900
1100
Impact Load (mN)

b)

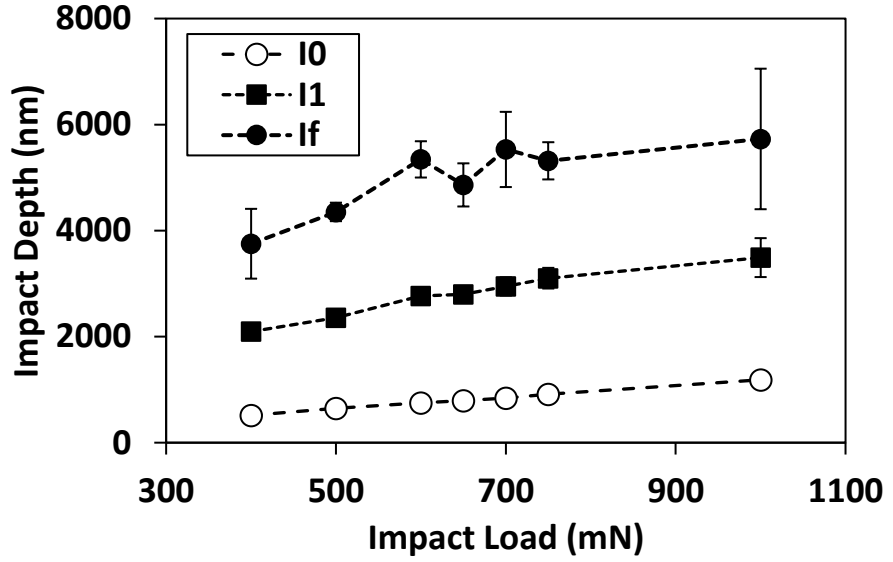
8000
6000
4000
2000
0
Impact Depth (nm)
I0
I1
If
300
500
700
900
1100
Impact Load (mN)

c)

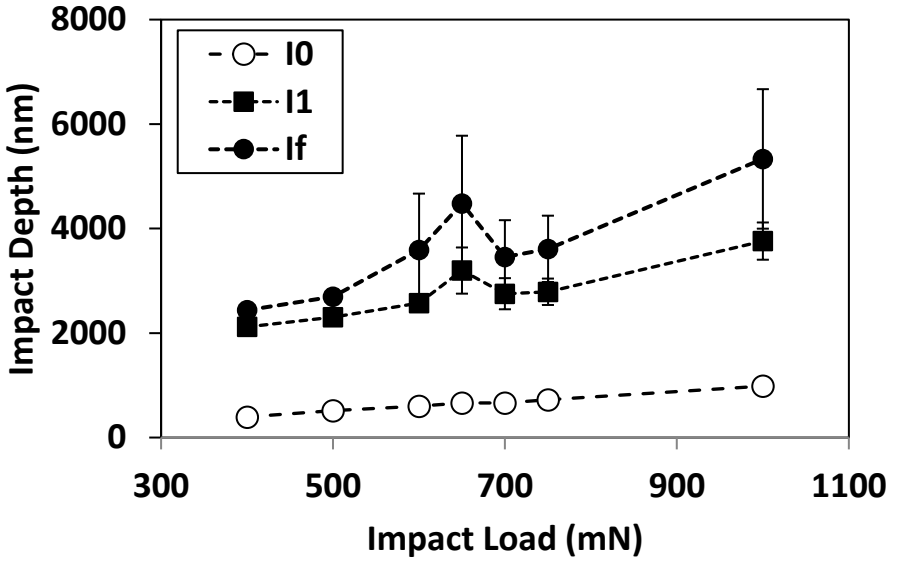
8000
6000
4000
2000
0
Impact Depth (nm)
I0
I1
If
300
500
700
900
1100
Impact Load (mN)

Figure 8. Impact parameters of coatings (I_0 – quasi-static depth, I_1 – depth of first true impact, I_f – depth of final impact) on HTS under micro-impact. A) Coating A b) Coating B c) Coating C.

The normalised difference in initial and final depth is shown in Figure 9 with the I_δ parameter. The use of this parameter simplifies the comparison of the impact depths and highlighting the performance of each coating the different loads. This allows the comparison of the impact and fatigue resistance of the coatings relative to each other. On HTS we can see that throughout the impact loads (Figure 8c)), Coating C remains at the lowest depth, achieving the smallest increase in depth thereby giving a low I_δ. Using this metric, a lower value is better, thereby suggesting Coating C as the best candidate for fatigue resistance. Though Coating A is seen to be better at lower load, it should be noted that raw depth reached through testing is greater giving it reduced impact resistance overall compared to Coating C.

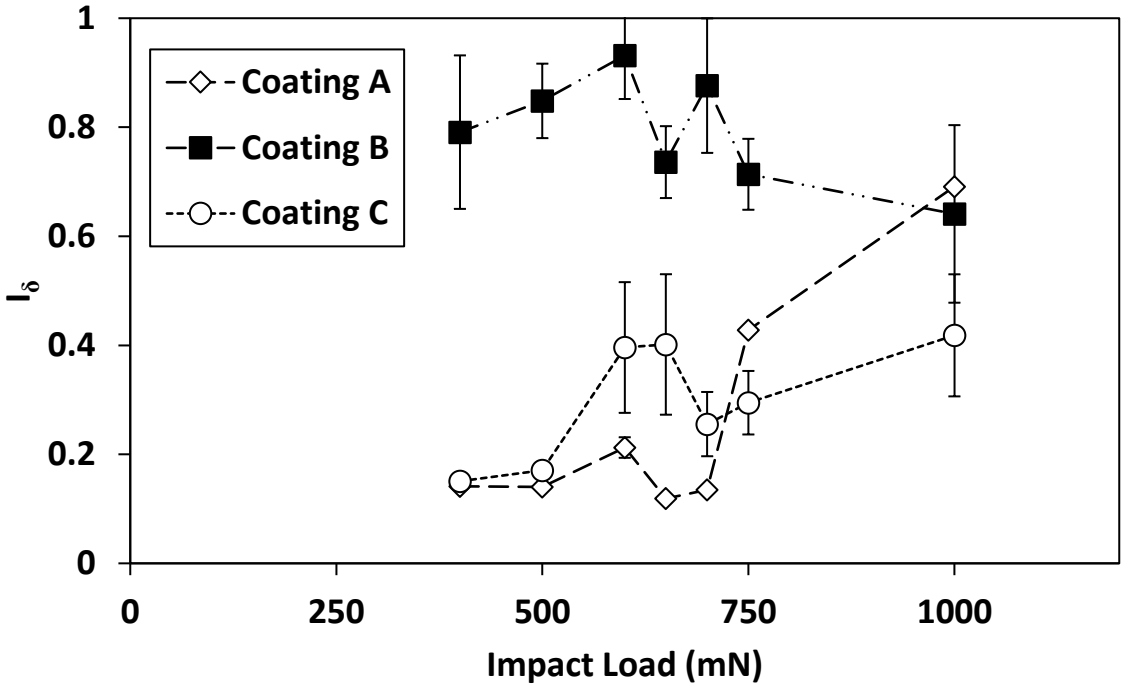

Figure 9**.** Graph of I_δ showing the change in depth from first impact to final impact normalized by initial depth to compare fatiguing of each coating on HTS.

Figure 10 demonstrates the differences in the cracking dynamics between Coating B and C on HTS. Coating B displays larger scale cracks permeating between the interlayer structure and top layer DLC. We can also see that the top layer DLC is almost entirely removed on the right side of the crater. These features indicate that this coating is more likely to crack and completely delaminate from the interlayer and substrate. In Coating C, a greater degree of cracking can be seen when compared to Coating B but the coating has not delaminated across any of the cross-sectioned area. Much of the cracks seen are intra-layer i.e. still within the same layer instead of causing layer removal. Smaller cracking phenomena such as this is more consistent with ductile failure wherein there are smaller crack areas but more are present [47].

a)

b)

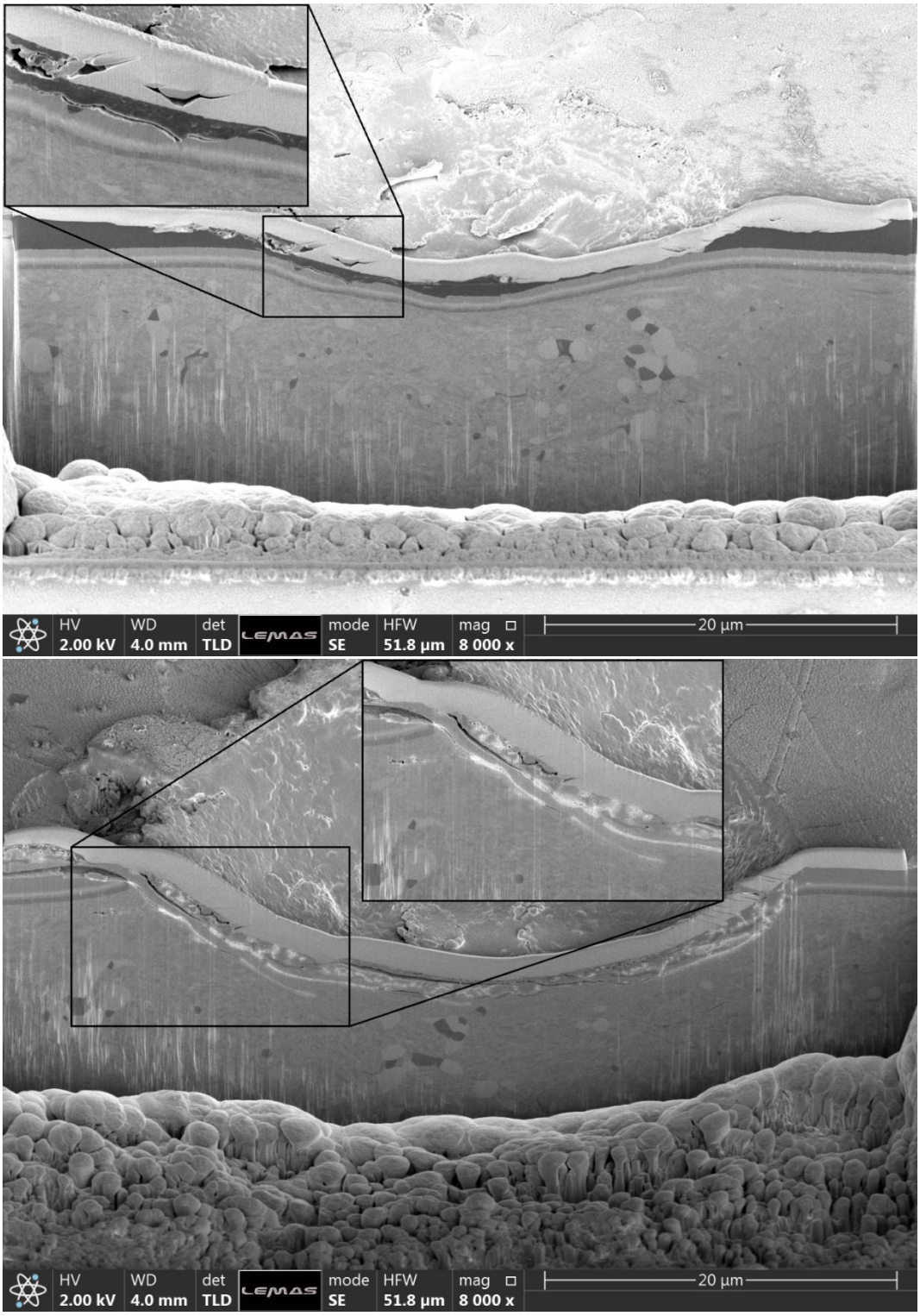

Figure 10. FIB-SEM cross section of 75 impacts at 1N load on a) Coating B and b) Coating C on HTS. Upper light material is platinum deposited before the FIB process.

3.5. Nano-impact analysis

The results of nano-impact testing shows the level of initial cracking of the coatings due to the smaller loads giving us less energy impact into the system with each impact. Figure 11 shows the progressive depth increase of Coatings A, B and C on both HTS and SS with 75 impacts at a load of 100 mN. Observing the difference in Figure 11 a) and b) under the same impact load, the deeper penetration in the SS coating is immediately apparent due to eggshell failure with the substrate unable to provide the necessary load support. As seen in Figure 11 and Table 7, Coating A on HTS has the smallest increase from I_1 (429 nm) to I_f (535 nm) resulting in an I_δ value of 0.18. Coating B is seen to have the largest increase in depth from 559 nm at I_1 to 917 nm at the end of testing giving an I_δ value of 0.64. Coating C has a more gradual increase in depth, though a higher value of I_1 of 661 nm, progressing to 910 nm. This gives an I_δ value of 0.38. Observing the I_δ values on the SS substrate, we see values that within the same range of the HTS substrate, however by the end of the impact testing only Coating A has not completely punctured all the coating layers with a final impact depth of approximately 2.05 µm compared to the total thickness of 2.78 µm. On SS, the top DLC layer of Coatings B and C are penetrated at first true impact (1.54 µm and 1.86 µm for I_1 with top DLC layers of 1.16 µm and 1.10 µm respectively). In addition to the relative depth increase in impact testing, the absolute depth relative to the coating thickness must be observed.

a)

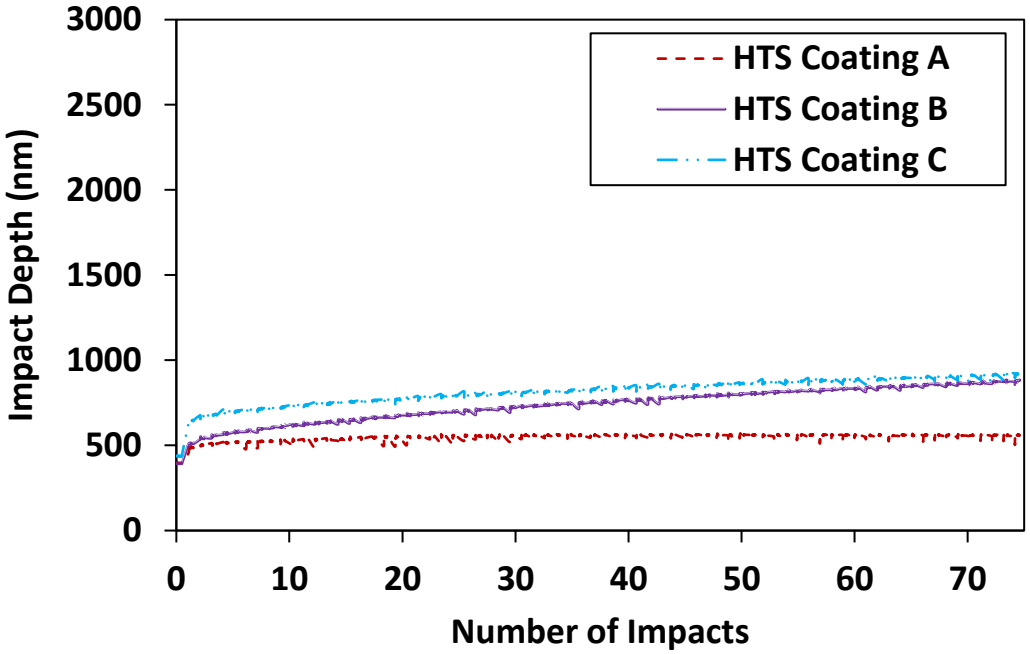

b)

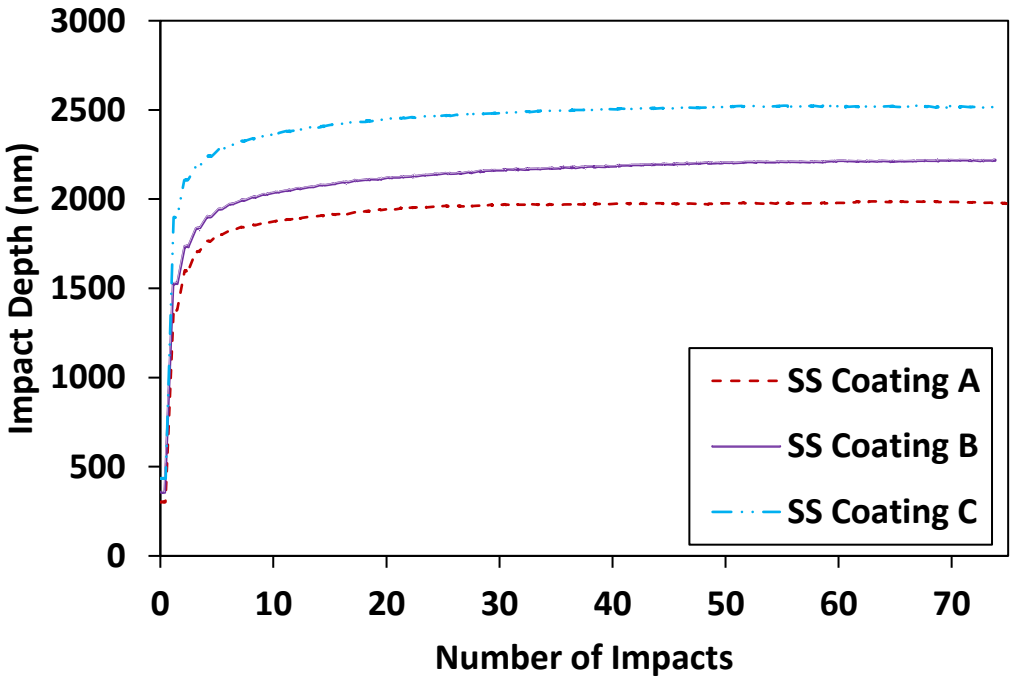

Figure 11. Representative nano-impact depth versus number of impacts for coatings A-C on a) HTS and b) SS. Impact load =100 mN. Total number of impacts = 75 (300 seconds of testing).

Table 7. Comparison of impact parameters (I_0 – quasi-static depth, I_1 – depth of first true impact, I_f – depth of final impact, I_δ – normalised difference between the first and final impact) in nano-impact tests at 100 mN load.

Substrate and Coating/Impact Parameter	I_0 (nm)	I_1 (nm)	I_f (nm)	I_δ
HTS Coating A	350 ± 23.0	429 ± 15.9	535 ± 31.8	0.18 ± 0.01
HTS Coating B	383 ± 28.8	559 ± 40.4	917 ± 66.3	0.64 ± 0.07
HTS Coating C	421 ± 25.5	661 ± 11.3	910 ± 9.93	0.38 ± 0.01
SS Coating A	327 ± 24.7	1402 ± 31.6	2058 ± 92.0	0.47 ± 0.02
SS Coating B	352 ± 16.7	1549 ± 28.1	2271 ± 65.8	0.47 ± 0.02
SS Coating C	420 ± 44.3	1864 ± 47.3	2511 ± 32.0	0.35 ± 0.01

3.6. Solid particle erosion

In Figure 12a), it is noted that the substrate exposure quickly climbs to approximately 100% for all coatings. At 5 seconds, all three coatings have completely failed by completing exposing the substrate, once again demonstrating the lessened load support of the SS substrate and showing the same behaviour between impact and erosion. Figure 12b) shows that Coating C can withstand erosive condition to a greater degree than Coatings A and B. After 400 seconds of solid particle impingement the substrate exposure is around 50 % compared to Coating A reaching 94 % at 210 seconds and Coating B reaching 97 % at 150 seconds. The substrate exposure value does vary throughout testing, but this is attributed to the small-scale cracking and deformation occurring on the surface of coating as opposed to the larger scale removal in the other coatings. As of the less substrate is exposed, this correlates with there being a larger layer of DLC remaining of the surface.

a)

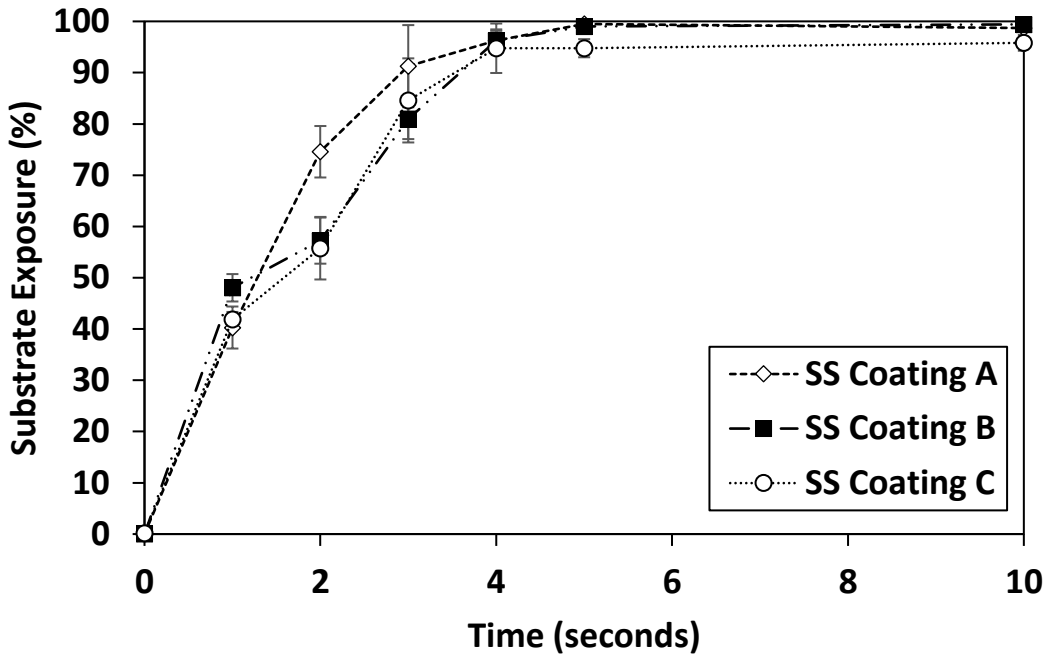

b)

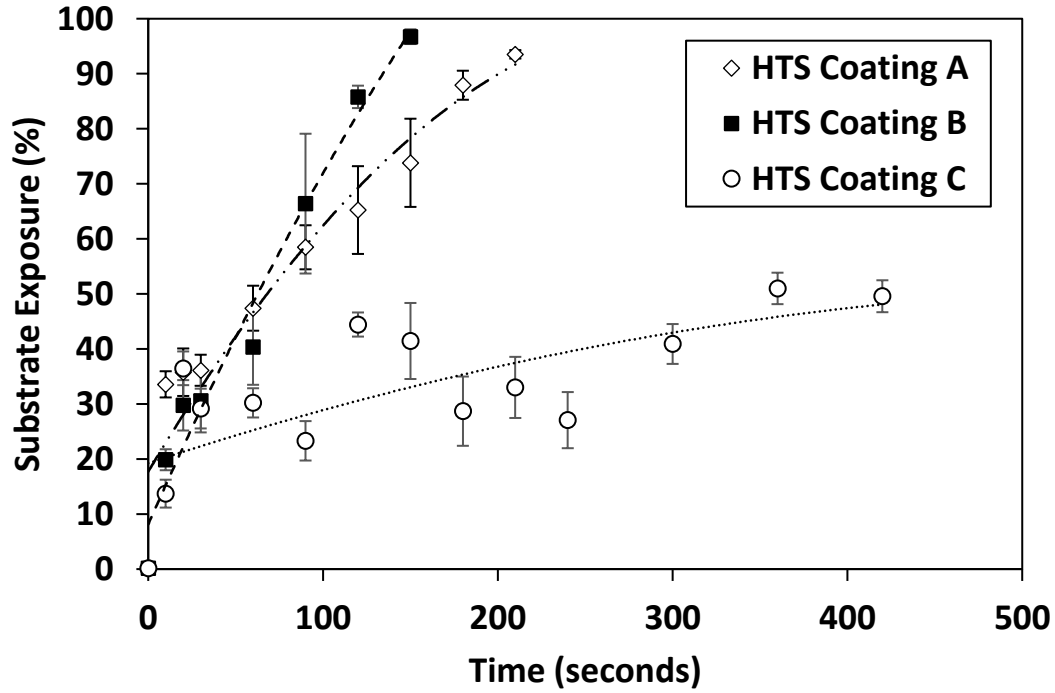

Figure 12. Substrate exposure of coatings on a) SS and b) HTS as measured by optical image analysis.

4. Discussion

4.1. On the significance of substrate hardness

Once a sufficient load-bearing substrate is present the fatigue resistance of the coating structure can be studied, by either instrumented impact or solid particle impingement. Marked differences are seen in the behaviour of the SS and HTS substrates under the same conditions as evidenced by Figure 7, Figure 11 and Figure 12. Higher depths are reached on SS under both micro and nano-impact with near instantaneous coatings failure seen under erosive conditions too.

This effect is known as egg-shelling (sometimes referred to as crème brûlée effect) where impact stress causes the coating structure collapse, presumed to collapse into the substrate due to it yielding and plastically deforming underneath the coating [76,78,79]. The softer SS substrate cannot support the stress induced by impact or erosion testing. This is further supported by sub-surface plastic deformation being common in impact wear [34]. The HTS substrate, therefore, allows for the analysis of the coating system in addition to giving a more fatigue resistant system due to the more consistent hardness and elastic modulus across the system as seen in Figure 4b) in comparison to Figure 4 a) where little drop in H/E ratio is seen with increase in depth. We can also note the higher surface hardness (10 GPa vs 2.6 GPa) and H/E and H^3/E^2 values (0.042 and 0.017 vs 0.012 GPa and 0.0004 GPa respectively) of HTS compared with SS in Table 3. It is interesting to note that SS has a higher Mean Elastic Modulus of 223 GPa compared with 204 GPa suggesting that stiffness alone does not benefit substrate support. The detrimental effects of low substrate hardness were also seen with investigation of erosion resistance on TiN coatings on tool steel [22]. Ramalingam and Zheng [80,81] noted that matching the elastic moduli of coatings and substrates will reduce tensile flexural stresses and therefore reduce film cracking alongside thicker coatings further reducing this stress . Therefore, it can be concluded coating fatigue resistance is first

controlled by the substrate's ability to support the coating structure and substrate properties must be considered for a well performing composite [82].

4.2. Coating Mechanical Properties

Nanoindentation and scratch tests were used to measure the nanomechanical properties and adhesion of the coatings. Using the measured mechanical properties [64,65] and scratch cracking parameters [66,67], we aim to predict the impact and erosion performance of the DLC coatings. Coating A possessed the highest hardness, H/E and H^3/E^2 (as seen in Table 3 and Figure 4, this can be attributed to the I_D/I_G ratio correlating with high sp^3 content [49]. Using the predictions of Leyland and Matthews [64] and Chen et al. [65], we would say this would predispose Coating A to have the best wear resistance as it would possess the highest elastic strain-to-break (~H/E) [32]. Further to this, metal ceramic coatings with high H^3/E^2 ratios performed well under impact conditions [39,83]. However, in the treatment of Lawn (and co-workers) and Pharr, fracture toughness follows an E/H (lower H/E) relationship thereby positioning Coating C to be the best performing with less change of fracture [32,64,84,85]. The difference in dependence in these parameters theoretically depends on influence of the applied stress and behaviour observed where crack resistance is benefitted by a low E or crack propagation where high stiffness would stop the cracking though a combination of these factors is probably at play [86]. The CPR_S provides valuable information on the predicted behaviour of the coatings too. On SS, Coating C is seen to have the highest CPR_S (Table 3) which can relate to the fracture toughness of the film [66,67]. The decrease in CPR_S in Coating C HTS can be explained by the change in the position of maximum stress due to the difference in coating thickness compared to the Coatings A and B [28].

Structural considerations must be made too. W doping in DLC films increases the sp^2 fraction of bonding present in the coating structure thereby giving it a more graphitic structure and softening the coating; clearly seen in Table 3 and Figure 4. The sp^2 ring structure and

presence of tungsten in its microstructure imparts a high elastic modulus to the coating while also giving it a lower surface hardness with the added likelihood of the presence of nanoscrystalline WC or W_2C [11,50,72,73,87]. Superior fatigue resistance is seen in tungsten doped DLC due to non-planar sp^2 carbon-carbon bonding allowing for greater compensation of shear stress [88]. The post impact results show a decrease in I_D/I_G corresponding to higher sp^3 content and destruction of larger sp^2 clusters [75]. There could also be a degree of hardening that occurs due to the Hall Petch effect or by compression of the nanocrystallites under impact [67,73,89]. Conversely, Si doping increases sp^3 fraction in a coating structure [13,90,91] however this doesn't result in a harder coating due to it developing a polymer like structure [92] and further softening with graphitisation (increase in I_D/I_G in Table 3) [74].

4.3. Micro- and Nano-impact

Multi-scale instrumented impact testing allows for varying strain rates and energies to be modelled in a method able to simulate fatigue conditions experienced in service far closer than other methods. It allows for individual impacts to be studied and for time to fail and on load depth to be measured [37,86]. Rueda-Ruiz et al. [35] recently showed that impact testing could be utilised to evaluate dynamic hardness at high strain rates. Due to the lower load and therefore lower strain, nano-impact allows us to see the initial repetitive strain resistance of the coatings. Figure 11a) and Table 7 suggest that initially Coating A on HTS performs better as the higher H^3/E^2 minimises plasticity [30]. This indicates initial load support in Coating A as also seen in the lower loads of micro-impact (Figure 9). In other nano/micro scale comparisons it is typical to change the probe geometry between length scales in order to drive failure rapidly [46], by maintaining the same probe throughout we can study the load dependent fatigue behaviour without pursuing film failure. We can also note that the comparison of the impact depths of HTS and SS seen in Figure 11 and Table 7 shows that egg-shelling also occurs in nano-impact.

Micro-impact allows for a far greater amount of energy to be fed into the system with greater loads for each impact. This allows for more dramatic failures to be seen and the loads to be parameterised to a greater degree as with Figure 8. The number of failures seen under multiple loads and repeats of the testing conditions (Table 6) compared with the depth parameters (Figure 8) and I_δ (Figure 9) show that throughout the testing Coating C has consistently performed the best with an overall lower impact depth at end of testing, lower impact depth increase during testing and less probability of failure within the given time [34]. Beake et al. [93] showed that impact testing could be used to probe the fracture toughness of ceramic coatings. It is noted in this paper that the fracture toughness follows an inverse relationship with the probe depth reached, further supporting Coating C as the superior architecture. Figure 7 demonstrates the full extent of eggshell failure between SS and HTS at micro-impact loads. Figure 10 gives greater insight into the cracking dynamics seen between Coatings B and C on HTS. Coating B has partly delaminated compared to Coating C where intralayer cracking is present. The cracked coating is still adhering to the surface. From this, we can gather that the multiple processes suggested earlier are seen with the lower *H/E* value and CPR_S benefitting fracture toughness and reducing the amount of crack propagation while the impact hardening benefits in fatigue resistance [32,84,86]. The reduced severity of cracking suggests a more semi-brittle nature rather than the brittle fracture seen in the other coatings.

4.4. Impact-Erosion link and wear resistance

Erosion tests with a bespoke air particle impingement jet showed that on HTS, Coating C had the most coating remaining on the surface and the least amount of substrate exposed (Figure 12), a combination of beneficial mechanical properties and the ability to structurally transform as seen under impact wear make this coating more erosive and fatigue resistant to particle impact. Repetitive impact induces fatiguing and fracture in materials intrinsically linking these processes [20–22,33,34,36–38]. Furthermore, Figure 9 and Figure 12 show a link in the

lowest increase in depth across the load range (with I_{δ}) and most coating remaining in erosion testing correlating to the a coating than is less likely to catastrophically crack and delaminate in either wear regime. Figure 10 corroborates this with less severe cracking seen within the coating layer. The same egg-shelling seen with micro- and nano-impact (Figure 7 and Figure 11 respectively) is seen under erosive conditions so that repetitive impacts either by sand particles or an indenter tip cause the coating structure collapse due to lack of substrate support [76,78,79]. Using all these parameters together it is possible to rank the relative performance under the repetitive fatigue conditions of impact and erosive wear, we can clearly see that Coating C is the superior coating for these wear regimes, followed by A and B on HTS as substrate support is first required. The use of a combination of nanomechanical techniques [32] paired with cross sectional SEM, to understand the cracking dynamics of coatings [59,60], can inform on how a specific coating structure behaves and how its properties drive different failure mechanisms (crack initiation or propagation) [32,84,86]. This is useful for other coatings beyond DLC where standardised instrumented impact can remove some of the randomness of erosion testing to make future coating architecture optimisation easier and the ranking of fatigue resistance possible.

5. Conclusion

Diamond-like carbon coatings were prepared on both 316L stainless steel and M2 tool steel by plasma assisted chemical vapour deposition. Nanoindentation was used to measure their mechanical properties relative to coating depth and Raman spectroscopy was used for structural characterisation. Multi-scale instrumented impact testing was used to compare fatigue resistance against erosion testing to find a link between the processes to allow for impact to be used as a more standardised method in future testing.

Correlation between the relative depth increase in instrumented impact and substrate exposure in erosion allows linking of the two wear processes and for the use of impact to inform fatigue

behaviour of coating under erosive conditions. The methodologies adopted in this paper can be applied to other coating architectures to assess their relative erosive and impact resistance to allow for future coating optimisation. Though it should be noted that a combination of techniques allows for a more complete characterisation of the behaviour of the system.

Differences in the relative fatigue resistance can be observed between coatings A, B and C correlating between erosion and impact testing. Coating C (with tungsten metallic doping) is seen to be the most resistant to fatigue wear due to its semi-brittle nature of smaller intralayer cracking. It follows that for DLC coatings, a lower *H/E* ratio is favourable for fatigue resistance. This lower *H/E* ratio correlates with increased toughness (~*E/H*) rather than elastic strain to break (~*H/E*). Additionally, impact and erosion testing shows that the resistance to wear in these two techniques is first dominated by the substrate's hardness and load bearing support, a harder substrate is most beneficial to fatigue resistance under repetitive loading conditions. The difference in hardness between the 316L stainless steel and DLC top layer is such that an eggshell type failure is seen under both impact and erosive wear.

Robust surface profilometry would allow for the amount of substrate exposure to be correlated to wear volume. Future studies could investigate the impact/erosion relation with thicker coatings or multi-top-layer coatings. Modelling to compare between the two methods and analyse the energy input into the system would allow for the fatigue behaviour to be further investigated. Additional post-test structural Raman and nanomechanical topographical mapping would allow for the dynamic structural transformation to be discerned as performed with fretting wear previously [40,41].

Acknowledgements

This work was supported by the Engineering and Physical Sciences Research Council (EPSRC), Grant No. ELP01629X and Micro Materials Ltd. as part of the EPSRC Doctoral

Training Centre in Integrated Tribology (iT-CDT). The authors would like to thank Stuart Micklethwaite of LEMAS (Leeds Electron Microscopy and Spectroscopy Centre producing the FIB-SEM cross sections and associated images.

References

[1] A. Grill, Diamond-like carbon: state of the art, Diam. Relat. Mater. 8 (1999) 428–434. doi:10.1016/S0925-9635(98)00262-3.

[2] J. Robertson, Diamond-like amorphous carbon, Mater. Sci. Eng. R Reports. 37 (2002) 129–281. doi:10.1016/S0927-796X(02)00005-0.

[3] S. V. Hainsworth, N.J. Uhure, Diamond like carbon coatings for tribology: production techniques, characterisation methods and applications, Int. Mater. Rev. 52 (2007) 153–174. doi:10.1179/174328007X160272.

[4] J. Robertson, Properties of diamond-like carbon, Surf. Coatings Technol. 50 (1992) 185–203. doi:10.1016/0257-8972(92)90001-Q.

[5] Y. Lifshitz, Diamond-like carbon — present status, Diam. Relat. Mater. 8 (1999) 1659–1676. doi:10.1016/S0925-9635(99)00087-4.

[6] A. Grill, Review of the tribology of diamond-like carbon, Wear. 168 (1993) 143–153. doi:10.1016/0043-1648(93)90210-D.

[7] W. Tillmann, N.F. Lopes Dias, D. Stangier, Tribo-mechanical properties of CrC/a-C thin films sequentially deposited by HiPIMS and mfMS, Surf. Coatings Technol. 335 (2018) 173–180. doi:10.1016/j.surfcoat.2017.12.035.

[8] M. Antonov, I. Hussainova, F. Sergejev, P. Kulu, A. Gregor, Assessment of gradient and nanogradient PVD coatings behaviour under erosive, abrasive and impact wear conditions, Wear. 267 (2009) 898–906. doi:10.1016/j.wear.2008.12.045.

[9] S. Yang, X. Li, N.M. Renevier, D.G. Teer, Tribological properties and wear mechanism of sputtered C/Cr coating, Surf. Coatings Technol. 142–144 (2001) 85–93. doi:10.1016/S0257-8972(01)01147-1.

[10] M. Diesselberg, H.R. Stock, P. Mayr, Friction and wear behaviour of PVD chromium nitride supported carbon coatings, Surf. Coatings Technol. 188–189 (2004) 612–616. doi:10.1016/j.surfcoat.2004.07.023.

[11] X. Chen, Z. Peng, Z. Fu, S. Wu, W. Yue, C. Wang, Microstructural, mechanical and tribological properties of tungsten-gradually doped diamond-like carbon films with functionally graded interlayers, Surf. Coatings Technol. 205 (2011) 3631–3638. doi:10.1016/j.surfcoat.2011.01.004.

[12] J.C. Sánchez-López, A. Fernández, Doping and alloying effects on DLC coatings, in: Tribol. Diamond-Like Carbon Film. Fundam. Appl., Springer US, Boston, MA, 2008: pp. 311–328. doi:10.1007/978-0-387-49891-1_12.

[13] J. Choi, M. Kawaguchi, T. Kato, M. Ikeyama, Deposition of Si-DLC film and its microstructural, tribological and corrosion properties, in: Microsyst. Technol., 2007: pp. 1353–1358. doi:10.1007/s00542-006-0368-8.

[14] K. Bewilogua, C. V. Cooper, C. Specht, J. Schröder, R. Wittorf, M. Grischke, Erratum to: `Effect of target material on deposition and properties of metal-containing DLC (Me-DLC) coatings' [Surf. Coat. Technol. 127 (2000) 224-234], Surf. Coatings Technol. 132 (2000) 275–283. doi:10.1016/S0257-8972(00)00746-5.

[15] B.D. Beake, T. Liskiewicz, Nanomechanical Characterization of Carbon Films, in: Appl. Nanoindentation Adv. Mater., 2017: pp. 19–68. doi:10.1002/9781119084501.ch2.

[16] T. Liskiewicz, A. Al-Borno, DLC Coatings in Oil and Gas Production, J. Coat. Sci.

Technol. 1 (2014) 59–68. doi:http://dx.doi.org/10.6000/2369-3355.2014.01.01.7.
[17] R.J.K. Wood, The sand erosion performance of coatings, Mater. Des. 20 (1999) 179–191. doi:10.1016/S0261-3069(99)00024-2.
[18] I.M. Hutchings, Ductile-brittle transitions and wear maps for the erosion and abrasion of brittle materials, J. Phys. D. Appl. Phys. 25 (1992) A212–A221. doi:10.1088/0022-3727/25/1A/033.
[19] J. Zahavi, G.F. Schmitt, Solid particle erosion of polymeric coatings, Wear. 71 (1981) 191–210. doi:10.1016/0043-1648(81)90338-0.
[20] A. Matthews, S. Franklin, K. Holmberg, Tribological coatings: Contact mechanisms and selection, J. Phys. D. Appl. Phys. 40 (2007) 5463–5475. doi:10.1088/0022-3727/40/18/S07.
[21] E. Bousser, L. Martinu, J.E. Klemberg-Sapieha, Solid particle erosion mechanisms of protective coatings for aerospace applications, Surf. Coatings Technol. 257 (2014) 165–181. doi:10.1016/j.surfcoat.2014.08.037.
[22] M. Bromark, P. Hedenqvist, S. Hogmark, The influence of substrate material on the erosion resistance of TiN coated tool steels, Wear. 186–187 (1995) 189–194. doi:10.1016/0043-1648(95)07163-6.
[23] B.S. Mann, V. Arya, A.K. Maiti, M.U.B. Rao, P. Joshi, Corrosion and erosion performance of HVOF/TiAlN PVD coatings and candidate materials for high pressure gate valve application, Wear. 260 (2006) 75–82. doi:10.1016/j.wear.2004.12.045.
[24] M.S. Mahdipoor, F. Tarasi, C. Moreau, A. Dolatabadi, M. Medraj, HVOF sprayed coatings of nano-agglomerated tungsten-carbide/cobalt powders for water droplet erosion application, Wear. 330–331 (2015) 338–347. doi:10.1016/j.wear.2015.02.034.
[25] M.W. Reedy, T.J. Eden, J.K. Potter, D.E. Wolfe, Erosion performance and characterization of nanolayer (Ti,Cr)N hard coatings for gas turbine engine compressor blade applications, Surf. Coatings Technol. 206 (2011) 464–472. doi:10.1016/j.surfcoat.2011.07.063.
[26] G. Barbezat, A.R. Nicol, A. Sickinger, Abrasion, erosion and scuffing resistance of carbide and oxide ceramic thermal sprayed coatings for different applications, Wear. 162–164 (1993) 529–537. doi:10.1016/0043-1648(93)90538-W.
[27] K.S. Tan, J.A. Wharton, R.J.K. Wood, Solid particle erosion-corrosion behaviour of a novel HVOF nickel aluminium bronze coating for marine applications - Correlation between mass loss and electrochemical measurements, in: Wear, Elsevier, 2005: pp. 629–640. doi:10.1016/j.wear.2004.02.019.
[28] X.C. Zhang, B.S. Xu, H.D. Wang, Y.X. Wu, Y. Jiang, Hertzian contact response of single-layer, functionally graded and sandwich coatings, Mater. Des. 28 (2007) 47–54. doi:10.1016/j.matdes.2005.06.018.
[29] S.J. Bull, Using work of indentation to predict erosion behavior in bulk materials and coatings, J. Phys. D. Appl. Phys. 39 (2006) 1626–1634. doi:10.1088/0022-3727/39/8/023.
[30] B.D. Beake, V.M. Vishnyakov, J.S. Colligon, Nano-impact testing of TiFeN and TiFeMoN films for dynamic toughness evaluation, J. Phys. D. Appl. Phys. 44 (2011). doi:10.1088/0022-3727/44/8/085301.
[31] K.-D. Bouzakis, G. Maliaris, S. Makrimallakis, Strain rate effect on the fatigue failure of thin PVD coatings: An investigation by a novel impact tester with adjustable repetitive force, Int. J. Fatigue. 44 (2012) 89–97. doi:10.1016/j.ijfatigue.2012.05.010.
[32] B.D. Beake, Evaluation of the fracture resistance of DLC coatings on tool steel under dynamic loading, Surf. Coatings Technol. 198 (2005) 90–93. doi:10.1016/j.surfcoat.2004.10.048.
[33] B.D. Beake, S.R. Goodes, J.F. Smith, R. Madani, C.A. Rego, R.I. Cherry, T. Wagner, Investigating the fracture resistance and adhesion of DLC films with micro-impact testing, Diam. Relat. Mater. 11 (2002) 1606–1609. doi:10.1016/S0925-9635(02)00107-

3.
[34] B.D. Beake, S.P. Lau, J.F. Smith, Evaluating the fracture properties and fatigue wear of tetrahedral amorphous carbon films on silicon by nano-impact testing, Surf. Coatings Technol. 177–178 (2004) 611–615. doi:10.1016/S0257-8972(03)00934-4.
[35] M. Rueda-Ruiz, B.D. Beake, J.M. Molina-Aldareguia, New instrumentation and analysis methodology for nano-impact testing, Mater. Des. (2020) 108715. doi:10.1016/j.matdes.2020.108715.
[36] B.D. Beake, T.W. Liskiewicz, A. Bird, X. Shi, Micro-scale impact testing - A new approach to studying fatigue resistance in hard carbon coatings, Tribol. Int. (2019). doi:10.1016/j.triboint.2019.04.016.
[37] B.D. Beake, S.R. Goodes, J.F. Smith, Micro-impact testing: A new technique for investigating thin film toughness, adhesion, erosive wear resistance, and dynamic hardness, Surf. Eng. 17 (2001) 187–192. doi:10.1179/026708401101517755.
[38] Q. Zhou, W. Han, Y. Du, H. Wu, A. Bird, X. Zhao, X. Wang, H. Wang, B.D. Beake, Enhancing fatigue wear resistance of a bulk metallic glass via introducing phase separation: A micro-impact test analysis, Wear. 436–437 (2019) 203037. doi:10.1016/J.WEAR.2019.203037.
[39] B.D. Beake, L. Isern, J.L. Endrino, G.S. Fox-Rabinovich, Micro-impact testing of AlTiN and TiAlCrN coatings, Wear. 418–419 (2019) 102–110. doi:10.1016/j.wear.2018.11.010.
[40] Y. Liu, T.W. Liskiewicz, B.D. Beake, Dynamic changes of mechanical properties induced by friction in the Archard wear model, Wear. 428–429 (2019) 366–375. doi:10.1016/j.wear.2019.04.004.
[41] T. Liskiewicz, K. Kubiak, T. Comyn, Nano-indentation mapping of fretting-induced surface layers, Tribol. Int. 108 (2017) 186–193. doi:10.1016/j.triboint.2016.10.018.
[42] Y. Lifshitz, G.D. Lempert, E. Grossman, I. Avigal, C. Uzan-Saguy, R. Kalish, J. Kulik, D. Marton, J.W. Rabalais, Growth mechanisms of DLC films from C + ions: experimental studies, Diam. Relat. Mater. 4 (1995) 318–323. doi:10.1016/0925-9635(94)05205-0.
[43] Z. Mala, T. Vitu, D. Novakova, Determination of coating thickness - industrial standard in the physics practical education, in: Phys. Teach. Eng. Educ., 2011: p. 4.
[44] W.C. Oliver, G.M. Pharr, An improved technique for determining hardness and elastic modulus using load and displacement sensing indentation experiments, J. Mater. Res. 7 (1992) 1564–1583. doi:10.1557/JMR.1992.1564.
[45] G.M. Pharr, W.C. Oliver, Measurement of thin film mechanical properties using nanoindentation, Mrs Bull. 17 (1992) 28–33. doi:10.1557/S0883769400041634.
[46] B.D. Beake, T.W. Liskiewicz, V.M. Vishnyakov, M.I. Davies, Development of DLC coating architectures for demanding functional surface applications through nano- and micro-mechanical testing, Surf. Coatings Technol. 284 (2015) 334–343. doi:10.1016/j.surfcoat.2015.05.050.
[47] S.J. Bull, Failure modes in scratch adhesion testing, Surf. Coatings Technol. 50 (1991) 25–32. doi:10.1016/0257-8972(91)90188-3.
[48] A. Ferrari, J. Robertson, Interpretation of Raman spectra of disordered and amorphous carbon, Phys. Rev. B - Condens. Matter Mater. Phys. 61 (2000) 14095–14107. doi:10.1103/PhysRevB.61.14095.
[49] F.C. Tai, S.C. Lee, C.H. Wei, S.L. Tyan, Correlation between ID/IG Ratio from Visible Raman Spectra and sp2/sp3 Ratio from XPS Spectra of Annealed Hydrogenated DLC Film, Mater. Trans. 47 (2006) 1847–1852. doi:10.2320/matertrans.47.1847.
[50] C. Rincón, G. Zambrano, A. Carvajal, P. Prieto, H. Galindo, E. Martínez, A. Lousa, J. Esteve, Tungsten carbide/diamond-like carbon multilayer coating on steel for tribological applications, Surf. Coatings Technol. 148 (2001) 277–283. doi:10.1016/S0257-8972(01)01360-3.

[51] A.C. Ferrari, J. Robertson, Raman spectroscopy of amorphous, nanostructured, diamond-like carbon, and nanodiamond, Philos. Trans. R. Soc. A Math. Phys. Eng. Sci. 362 (2004) 2477–2512. doi:10.1098/rsta.2004.1452.
[52] A.C. Ferrari, Determination of bonding in diamond-like carbon by Raman spectroscopy, Diam. Relat. Mater. 11 (2002) 1053–1061. doi:10.1016/S0925-9635(01)00730-0.
[53] C. Casiraghi, F. Piazza, A.C. Ferrari, D. Grambole, Bonding in hydrogenated diamond-like carbon by Raman spectroscopy, Diam. Relat. Mater. 14 (2005) 1098–1102. doi:10.1016/J.DIAMOND.2004.10.030.
[54] M. Born, E. Wolf, Principles of optics : electromagnetic theory of propagation, interference and diffraction of light, Pergamon, 1999.
[55] J.B. Zu, G.T. Burstein, I.M. Hutchings, A comparative study of the slurry erosion and free-fall particle erosion of aluminium, Wear. 149 (1991) 73–84. doi:10.1016/0043-1648(91)90365-2.
[56] I.M. Hutchings, A model for the erosion of metals by spherical particles at normal incidence., ,. 70 (1981) 269–281. doi:10.1016/0043-1648(81)90347-1.
[57] A.W. Ruff, S.. Wiederhorn, Erosion by solid particle impact, Treatise Mater. Sci. Technol. 16 (1979) 69–126. http://www.dtic.mil/docs/citations/ADA066525 (accessed July 13, 2018).
[58] K.-D. Bouzakis, A. Siganos, T. Leyendecker, G. Erkens, Thin hard coatings fracture propagation during the impact test, Thin Solid Films. 460 (2004) 181–189. doi:10.1016/j.tsf.2004.02.009.
[59] M.F. Bin Abdollah, Y. Yamaguchi, T. Akao, N. Inayoshi, N. Miyamoto, T. Tokoroyama, N. Umehara, Deformation-wear transition map of DLC coating under cyclic impact loading, Wear. 274–275 (2012) 435–441. doi:10.1016/j.wear.2011.11.007.
[60] M.F. Bin Abdollah, Y. Yamaguchi, T. Akao, N. Inayoshi, T. Tokoroyama, N. Umehara, The Effect of Maximum Normal Impact Load, Absorbed Energy, and Contact Impulse, on the Impact Crater Volume/Depth of DLC Coating, Tribol. Online. 6 (2011) 257–264. doi:10.2474/trol.6.257.
[61] A.C. Fischer-Cripps, Critical review of analysis and interpretation of nanoindentation test data, Surf. Coatings Technol. 200 (2006) 4153–4165. doi:10.1016/j.surfcoat.2005.03.018.
[62] L. Ward, F. Junge, A. Lampka, M. Dobbertin, C. Mewes, M. Wienecke, The Effect of Bias Voltage and Gas Pressure on the Structure, Adhesion and Wear Behavior of Diamond Like Carbon (DLC) Coatings With Si Interlayers, Coatings. 4 (2014) 214–230. doi:10.3390/coatings4020214.
[63] P.J. Wilbur, J.A. Davis, R. Wei, J.J. Vajo, D.L. Williamson, High current density, low energy, ion implantation of AISI-M2 tool steel for tribological applications, Surf. Coatings Technol. 83 (1996) 250–256. doi:10.1016/0257-8972(95)02830-7.
[64] A. Leyland, A. Matthews, On the significance of the H/E ratio in wear control: A nanocomposite coating approach to optimised tribological behaviour, Wear. 246 (2000) 1–11. doi:10.1016/S0043-1648(00)00488-9.
[65] X. Chen, Y. Du, Y.W. Chung, Commentary on using H/E and H3/E2 as proxies for fracture toughness of hard coatings, Thin Solid Films. (2019). doi:10.1016/j.tsf.2019.04.040.
[66] G.S. Fox-Rabinovich, B.D. Beake, J.L. Endrino, S.C. Veldhuis, R. Parkinson, L.S. Shuster, M.S. Migranov, Effect of mechanical properties measured at room and elevated temperatures on the wear resistance of cutting tools with TiAlN and AlCrN coatings, Surf. Coatings Technol. 200 (2006) 5738–5742. doi:10.1016/j.surfcoat.2005.08.132.
[67] S. Zhang, D. Sun, Y. Fu, H. Du, Effect of sputtering target power on microstructure

and mechanical properties of nanocomposite nc-TiN/a-SiNx thin films, in: Thin Solid Films, Elsevier, 2004: pp. 462–467. doi:10.1016/S0040-6090(03)01125-8.
[68] Y. Xia, M. Bigerelle, J. Marteau, P.E. Mazeran, S. Bouvier, A. Iost, Effect of surface roughness in the determination of the mechanical properties of material using nanoindentation test, Scanning. 36 (2014) 134–149. doi:10.1002/sca.21111.
[69] A.M. Korsunsky, M.R. McGurk, S.J. Bull, T.F. Page, On the hardness of coated systems, Surf. Coatings Technol. 99 (1998) 171–183. doi:10.1016/S0257-8972(97)00522-7.
[70] W.G. Jiang, J.J. Su, X.Q. Feng, Effect of surface roughness on nanoindentation test of thin films, Eng. Fract. Mech. 75 (2008) 4965–4972. doi:10.1016/j.engfracmech.2008.06.016.
[71] J.I. Goldstein, D.E. Newbury, J.R. Michael, N.W.M. Ritchie, J.H.J. Scott, D.C. Joy, Scanning electron microscopy and x-ray microanalysis, Springer New York, 2017. doi:10.1007/978-1-4939-6676-9.
[72] Q. Yong, G. Ma, H. Wang, S. Chen, B. Xu, Influence of tungsten content on microstructure and properties of tungsten-doped graphite-like carbon films, J. Mater. Res. 31 (2016) 3766–3776. doi:10.1557/jmr.2016.433.
[73] Y.T. Pei, D. Galvan, J.T.M. De Hosson, Nanostructure and properties of TiC/a-C:H composite coatings, Acta Mater. 53 (2005) 4505–4521. doi:10.1016/j.actamat.2005.05.045.
[74] P.E. Hovsepian, P. Mandal, A.P. Ehiasarian, G. Sáfrán, R. Tietema, D. Doerwald, Friction and wear behaviour of Mo-W doped carbon-based coating during boundary lubricated sliding, Appl. Surf. Sci. 366 (2016) 260–274. doi:10.1016/j.apsusc.2016.01.007.
[75] M.F. Bin Abdollah, Y. Yamaguchi, T. Akao, N. Inayoshi, N. Umehara, T. Tokoroyama, Phase transformation studies on the a-C coating under repetitive impacts, Surf. Coatings Technol. 205 (2010) 625–631. doi:10.1016/j.surfcoat.2010.07.062.
[76] M.D. Bentzon, K. Mogensen, J.B. Hansen, C. Barholm-Hansen, C. Træholt, P. Holiday, S.S. Eskildsen, Metallic interlayers between steel and diamond-like carbon, Surf. Coatings Technol. 68–69 (1994) 651–655. doi:10.1016/0257-8972(94)90232-1.
[77] B.D. Beake, S.J. McMaster, T.W. Liskiewicz, A. Neville, Influence of Si and W doping on impact resistance of DLC coatings on hardened steel, (n.d.).
[78] Z. Hu, A. Schubnov, F. Vollertsen, Tribological behaviour of DLC-films and their application in micro deep drawing, J. Mater. Process. Technol. 212 (2012) 647–652. doi:10.1016/j.jmatprotec.2011.10.012.
[79] T. Wright, T.F. Page, Nanoindentation and microindentation studies of hard carbon on 304 stainless steel, Surf. Coatings Technol. 54–55 (1992) 557–562. doi:10.1016/S0257-8972(07)80082-X.
[80] L. Zheng, S. Ramalingam, Multi-layer and composite structures for advanced coatings, Surf. Coatings Technol. 81 (1996) 52–71. doi:10.1016/0257-8972(95)02618-5.
[81] S. Ramalingam, L. Zheng, Film-substrate interface stresses and their role in the tribological performance of surface coatings, Tribol. Int. 28 (1995) 145–161. doi:10.1016/0301-679X(95)98963-E.
[82] J. Meneve, K. Vercammen, E. Dekempeneer, J. Smeets, Thin tribological coatings: Magic or design?, Surf. Coatings Technol. 94–95 (1997) 476–482. doi:10.1016/S0257-8972(97)00430-1.
[83] J. Chen, H. Li, B.D. Beake, Load sensitivity in repetitive nano-impact testing of TiN and AlTiN coatings, Surf. Coatings Technol. 308 (2016) 289–297. doi:10.1016/j.surfcoat.2016.05.094.
[84] G.R. ANSTIS, P. CHANTIKUL, B.R. LAWN, D.B. MARSHALL, A Critical Evaluation of Indentation Techniques for Measuring Fracture Toughness: I, Direct Crack Measurements, J. Am. Ceram. Soc. 64 (1981) 533–538. doi:10.1111/j.1151-

2916.1981.tb10320.x.
[85] G.M. Pharr, Measurement of mechanical properties by ultra-low load indentation, Mater. Sci. Eng. A. 253 (1998) 151–159. doi:10.1016/s0921-5093(98)00724-2.
[86] B.D. Beake, J.F. Smith, Nano-impact testing - An effective tool for assessing the resistance of advanced wear-resistant coatings to fatigue failure and delamination, Surf. Coatings Technol. 188–189 (2004) 594–598. doi:10.1016/j.surfcoat.2004.07.016.
[87] W. Yue, C. Liu, Z. Fu, C. Wang, H. Huang, J. Liu, Effects of tungsten doping contents on tribological behaviors of tungsten-doped diamond-like carbon coatings lubricated by MoDTC, Tribol. Lett. 58 (2015) 1–10. doi:10.1007/s11249-015-0508-3.
[88] S. Soltanahmadi, T. Charpentier, I. Nedelcu, V. Khetan, A. Morina, H.M. Freeman, A.P. Brown, R. Brydson, M.C.P. Van Eijk, A. Neville, Surface Fatigue Behavior of a WC/aC:H Thin-Film and the Tribochemical Impact of Zinc Dialkyldithiophosphate, ACS Appl. Mater. Interfaces. 11 (2019) 41676–41687. doi:10.1021/acsami.9b14669.
[89] J. Rao, T. Rose, M. Craig, J.R. Nicholls, Wear coatings for high load applications, in: Procedia CIRP, 2014: pp. 277–280. doi:10.1016/j.procir.2014.07.005.
[90] A.A. Ogwu, R.W. Lamberton, S. Morley, P. Maguire, J. McLaughlin, Characterization of thermally annealed diamond like carbon (DLC) and silicon modified DLC films by Raman spectroscopy, Phys. B Condens. Matter. 269 (1999) 335–344. doi:10.1016/S0921-4526(99)00138-6.
[91] S.C. Ray, W.F. Pong, P. Papakonstantinou, Iron, nitrogen and silicon doped diamond like carbon (DLC) thin films: A comparative study, Thin Solid Films. 610 (2016) 42–47. doi:10.1016/j.tsf.2016.04.048.
[92] W.J. Wu, M.H. Hon, The structure and residual stress in Si containing diamond-like carbon coating, Thin Solid Films. 307 (1997) 1–5. doi:10.1016/S0040-6090(97)00251-4.
[93] B.D. Beake, J.F. Smith, M.J. s. I. García, Micro-impact testing: A new technique for investigating fracture toughness, Thin Solid Films. 398–399 (2001) 438–443. doi:10.1016/S0040-6090(01)01397-9.